



1 **Observationally constrained analysis of sulfur cycle in the marine atmosphere with NASA**  
2 **ATom measurements and AeroCom model simulations**

3  
4 Huisheng Bian<sup>1,2</sup>, Mian Chin<sup>2</sup>, Peter R. Colarco<sup>2</sup>, Eric C. Apel<sup>3</sup>, Donald R. Blake<sup>4</sup>, Karl Froyd<sup>5</sup>, Rebecca S.  
5 Hornbrook<sup>3</sup>, Jose Jimenez<sup>6,5</sup>, Pedro Campuzano Jost<sup>6,5</sup>, Michael Lawler<sup>5,7</sup>, Mingxu Liu<sup>8</sup>, Marianne Tronstad Lund<sup>9</sup>,  
6 Hitoshi Matsui<sup>8</sup>, Benjamin A. Nault<sup>6,5,10,11</sup>, Joyce E. Penner<sup>12</sup>, Andrew W. Rollins<sup>5,13</sup>, Gregory Schill<sup>7</sup>, Ragnhild B.  
7 Skeie<sup>9</sup>, Hailong Wang<sup>14</sup>, Lu Xu<sup>15,16</sup>, Kai Zhang<sup>14</sup>, and Jialei Zhu<sup>17</sup>

8  
9 <sup>1</sup>Goddard Earth Sciences Technology and Research (GESTAR) II, University of Maryland at Baltimore County,  
10 Baltimore, MD, USA.

11 <sup>2</sup>NASA Goddard Space Flight Center, Greenbelt, MD, USA.

12 <sup>3</sup>Atmospheric Chemistry Observations & Modeling Laboratory, National Center for Atmospheric Research,  
13 Boulder, CO, USA,

14 <sup>4</sup>Department of Chemistry, University of California Irvine, CA, USA.

15 <sup>5</sup>Cooperative Institute for Research in Environmental Sciences, University of Colorado, Boulder, CO, USA.

16 <sup>6</sup>Department of Chemistry, University of Colorado, Boulder, CO, USA.

17 <sup>7</sup>NOAA Chemical Sciences Laboratory, Boulder, CO, USA.

18 <sup>8</sup>Graduate School of Environmental Studies, Nagoya University, Nagoya, Japan.

19 <sup>9</sup>CICERO Center for International Climate Research, Oslo, Norway.

20 <sup>10</sup>Now at: Department of Environmental Health and Engineering, Whiting School of Engineering, The Johns  
21 Hopkins, Baltimore, MD, USA

22 <sup>11</sup>Now at: Center for Aerosol and Cloud Chemistry, Aerodyne Research, Inc., Billerica, MA, USA

23 <sup>12</sup>Dept. of Atmospheric, Oceanic and Space Sciences, University of Michigan, Ann Arbor, Michigan, USA.

24 <sup>13</sup>NOAA Earth System Research Laboratory, Chemical Sciences Division, Boulder, CO, USA.

25 <sup>14</sup>Atmospheric Sciences and Global Change Division, Pacific Northwest National Laboratory, Richland, WA, USA.

26 <sup>15</sup>Division of Geological and Planetary Sciences, California Institute of Technology, Pasadena, CA, USA.

27 <sup>16</sup>Now at Department of Energy, Environmental and Chemical Engineering, Washington University in St. Louis,  
28 Missouri, USA.

29 <sup>17</sup>Institute of Surface-Earth System Science, School of Earth System Science, Tianjin University, Tianjin, China.

30  
31 *Correspondence to:* Huisheng Bian ([huisheng.bian@nasa.gov](mailto:huisheng.bian@nasa.gov))

32  
33 **Abstract**

34 The sulfur cycle plays a key role in atmospheric air quality, climate, and ecosystems. In this  
35 study, we compare the spatial and temporal distribution of four sulfur-containing species,  
36 dimethyl sulfide (DMS), sulfur dioxide (SO<sub>2</sub>), particulate methanesulfonate (MSA), and  
37 particulate sulfate (SO<sub>4</sub>), that were measured during the airborne NASA Atmospheric  
38 Tomography (ATom) mission and simulated by five AeroCom-III models to analyze the budget  
39 of sulfur cycle from the models. This study focuses on remote regions over the Pacific, Atlantic,  
40 and Southern Oceans from near the ocean surface to ~12-km altitude range, and covers all four  
41 seasons. These regions provide us with highly heterogeneous natural and anthropogenic source  
42 environments, which is not usually the case for traditional continental studies. We examine the  
43 vertical and seasonal variations of these sulfur species over tropical, mid-, and high-latitude  
44 regions in both hemispheres. We identify their origins from land versus ocean and from  
45 anthropogenic versus natural sources with sensitivity studies by applying tagged tracers linking  
46 to emission types and regions. In general, the differences among model results can be greater  
47 than one-order of magnitude. Comparing with observations, simulated SO<sub>2</sub> is generally low  
48 while SO<sub>4</sub> is high, and the model-observation agreement is much better in ATom-4 (April-May,  
49 2018). There are much larger DMS concentrations simulated close to the sea surface than  
50 observed, indicating that the DMS emissions may be too high from all models. Anthropogenic  
51 emissions are the dominant source (40–60% of the total amount) for atmospheric sulfate



52 simulated at locations and times along the ATom flight tracks at almost every altitude, followed  
53 by volcanic emissions (18-32%) and oceanic sources (16-32%). Similar source contributions can  
54 also be derived at broad ocean basin and monthly scales, indicating that any reductions of  
55 anthropogenic sulfur emissions would have global impacts in modern times.

## 56 57 **1. Introduction**

58 Atmospheric sulfur species have wide-ranging environmental and health impacts. About two-  
59 third of sulfur emissions come from anthropogenic activities (Chin et al., 2000); therefore,  
60 considerable efforts have been made to reduce these sulfur emissions. For example, acid rain  
61 occurs when sulfur dioxide ( $\text{SO}_2$ ) is oxidized to form sulfuric acid and particulate sulfate ( $\text{SO}_4$ ),  
62 which fall to the ground with the rain (Bian et al., 1993; Grennfelt et al., 2020) and can wreak  
63 havoc on aquatic ecosystems (Josephson et al., 2014; McDonnell et al., 2021). Through the  
64 competing neutralization reaction of  $\text{SO}_4$  and nitrate with  $\text{NH}_3$  and other alkaline species,  $\text{SO}_4$   
65 affects strongly both particulate nitrate formation (Bian et al., 2017) and aerosol pH (Huang et  
66 al., 2020; Nault et al., 2021). Sulfate is a key component of particulate matter (PM), which  
67 degrades air quality (Dong et al., 2018; Tan et al., 2018) and directly reflects the sun's rays  
68 (Moch et al., 2022; Myhre et al., 2013). Due to its highly hygroscopic nature, sulfate aerosol  
69 affects cloud physics (Boucher et al., 2013; Breen et al., 2021; Seinfeld et al., 2016) and thus  
70 indirectly radiative forcing (Penner et al., 2016; Wang et al., 2021) through aerosol-cloud  
71 interactions. The contribution of aerosols to atmospheric clouds and energy budget remains the  
72 largest uncertainty in climate models (Gryspeerd et al., 2023; Jia et al., 2021, 2022; Klein et al.,  
73 2013; Malavelle et al., 2017).

74  
75 Unlike other major atmospheric aerosols, a significant fraction (i.e., roughly a quarter) of sulfate  
76 in the atmosphere comes from marine biological emissions (Chin et al., 1996). The impact of  
77 oceanic sulfate is particularly pronounced on marine shallow clouds, which are characterized by  
78 low droplet number concentrations and weak updraft velocities (Rissman et al., 2004). Sulfur  
79 research has also focused on the tropical upper troposphere (TUT), where the growth of new  
80 aerosol particles and homogeneous nucleation involving sulfuric acid is at a maximum  
81 (Williamson et al., 2019), and where deep convective transport allows a small portion of the  
82 sources to reach the lower stratosphere. The resulting sulfate aerosols in the stratosphere can  
83 persist for years (Holton et al., 1995). Unfortunately, the TUT and above are observation-sparse  
84 regions. Acquiring atmospheric composition and its chemical/physical properties over remote  
85 oceans is challenging, although satellites can often provide total column constraints of aerosol  
86 optical depth.

87  
88 The NASA Earth Venture Suborbital (EVS-2) Atmospheric Tomography (ATom) airborne  
89 mission provided abundant measurements of gases and aerosols over the world's oceans (Hodzic  
90 et al., 2020; Thompson et al., 2021). In particular, a suite of instruments integrated on the NASA  
91 DC-8 aircraft made measurements of many important sulfur species including dimethyl sulfide  
92 (DMS),  $\text{SO}_2$ , particulate methanesulfonate (MSA) and  $\text{SO}_4$  over the Pacific and Atlantic Oceans  
93 in both hemispheres and the Southern Ocean in all four seasons. This comprehensive sulfur  
94 dataset provides us with unprecedented opportunities to assess sulfur source, transport,  
95 chemistry, deposition, and particle activation and growth represented in the global aerosol  
96 models, and to estimate the extent of anthropogenic influence on remote oceanic atmospheric  
97 composition and cloud properties.



98  
99 This study has two specific scientific goals. First, we explore the vertical and seasonal variation  
100 of sulfur species (i.e., DMS, SO<sub>2</sub>, MSA, and SO<sub>4</sub>) using ATom measurements and simulations  
101 from five global models that participated in the AeroCom-ATom model experiments. AeroCom  
102 is an international initiative of scientists aiming at the advancement of the understanding of the  
103 global aerosol and its impact on climate (<https://aerocom.met.no/>). Here we focus on remote  
104 regions over the Pacific, Atlantic, and Southern Oceans, from near the surface to an altitude of  
105 about 12 kilometers, covering all four seasons. Second, we determine whether the produced SO<sub>4</sub>  
106 originated from land or ocean sources and from anthropogenic or natural sources by using tagged  
107 tracers associated with emission types and regions.

108  
109 The structure of this paper is as follows. Section 2 describes the ATom measurements and the  
110 AeroCom models used in this study. Section 3 presents the ATom-AeroCom sulfur comparison  
111 from different perspectives, namely the overall comparison in Sect. 3.1, the vertical profiles in  
112 Sect. 3.2, and the regional and seasonal analysis in Sect. 3.3. The sulfur budget analysis is given  
113 in Sect. 4. We further present investigations of source origins for aerosol SO<sub>4</sub> along flight tracks  
114 and over oceans in Sect. 5. Finally, we summarize our findings in Sect. 6.

## 115 116 **2. Data**

### 117 **2.1 ATom measurements**

118 ATom was a NASA-funded Earth Venture Suborbital project designed to study the effects of air  
119 pollution on chemically reactive gases, aerosols, and greenhouse gases in the remote atmosphere.  
120 ATom deployed a large suite of gas and aerosol measurement instruments on the NASA DC-8  
121 aircraft for systematic sampling, covering an extended region of the globe from 85°N to 85°S  
122 over the Pacific and Atlantic Oceans, with vertical profiles from near-surface to near-tropopause  
123 (i.e., ~0.2-12 km) (Thompson et al., 2021). Four ATom deployments (ATom-1 to -4) were  
124 executed over each of the four seasons from 2016 to 2018, and their flight paths are shown in  
125 Fig. 1. The extensive aerosol and gas measurements made during ATom include inorganic and  
126 organic aerosols, precursor gases, particle size distributions and particle composition. Table 1  
127 lists the instruments for ATom sulfur species observations used in this study including the  
128 relevant sampling details needed for the model comparison.

129  
130 We use SO<sub>4</sub> and MSA that had been measured by two instruments, the University of Colorado  
131 Aerodyne high-resolution time-of-flight aerosol mass spectrometer (AMS, Canagaratna et al.,  
132 2007; Guo et al., 2021), and the NOAA Particle Analysis by Laser Mass Spectrometry (PALMS,  
133 Froyd et al., 2019). The latter one makes in situ measurements of the chemical composition of  
134 individual aerosol particles. Furthermore, AMS measured submicron aerosols while PALMS  
135 provided mass mixing ratio and size distribution up to 3 μm in dry diameter (Brock et al., 2019).  
136 It is worth noting that AMS data were independently processed and reported at both 1-s and 60-s  
137 time resolutions by instrument PI (Jimenez et al., 2019). The detection limit varied with different  
138 averaging time resolutions, and they were provided directly for each sampling point in AMS  
139 datasets. Some negative measurements were also presented in AMS datasets, and this is normal  
140 for measurements of very low concentrations in the presence of instrumental noise. The AMS  
141 data at 60-s resolution is recommended owing to more robust peak fitting at low concentrations  
142 (Hodzic et al., 2020). Given the complex data overlays (i.e., starting, ending, and frequency)  
143 reported from multiple instruments, the ATom team also provide a 10-s merged dataset to



144 facilitate users' applications. In this study, we evaluate data reported in different time  
145 resolutions, using AMS as an example, to ensure the quality of merged data that are exclusively  
146 used as the primary dataset in this work.

147  
148 Two instruments, the California Institute of Technology Chemical Ionization Mass Spectrometer  
149 (CIMS) and the NOAA Laser Induced Fluorescence (LIF), were used for SO<sub>2</sub> measurements  
150 (Table 1). The CIMS uses CF<sub>3</sub>O<sup>-</sup> as a reagent ion which reacts with SO<sub>2</sub> via fluoride ion transfer  
151 chemistry. The product ion is detected by a compact time-of-flight mass spectrometer (CToF).  
152 The precision of the CIMS SO<sub>2</sub> measurement decreases with increasing water vapor  
153 concentration (Eger et al., 2019; Huey et al., 2004; Jurkat et al., 2016; Rickly et al., 2021),  
154 making it challenging to measure SO<sub>2</sub> in remote ocean regions. In these regions, the ambient  
155 water vapor may be sufficiently high that the CIMS SO<sub>2</sub> precision at 1-s resolution (~130 parts  
156 per trillion by volume, pptv) is insufficient for measuring ambient SO<sub>2</sub> value there (<100 pptv).  
157 To address this shortcoming, the ATom science team added a new instrument, the NOAA LIF, to  
158 the ATom-4 payload. The NOAA LIF instrument uses red-shifted laser-induced fluorescence to  
159 detect SO<sub>2</sub> at very low ppt levels (Rickly et al., 2021; Rollins et al., 2016). Both instruments  
160 report negative values and the detection limit of the LIF instrument is about 2 pptv.

161  
162 DMS was measured during ATom by two instruments, the University of California, Irvine  
163 Whole Air Sampler (WAS), and the NCAR Trace Organic Gas Analyzer (TOGA). The WAS  
164 reported DMS for all four ATom deployments, while the TOGA reported data for ATom-2 to -4  
165 and not for ATom-1 due to possible issues associated with the TOGA inlet (the inlet was  
166 changed for ATom-2 to -4). Both instruments have comparable detection limit (1 pptv) and  
167 accuracy (~15%). However, the sampling time interval of WAS (variable but ~180s) was longer  
168 than TOGA (~120s).

## 169 170 **2.2 AeroCom models**

171 Five global aerosol models participated in an AeroCom-ATom model experiment  
172 (<https://wiki.met.no/aerocom/phase3-experiments>): CAM-ATRAS, E3SM, GEOS, IMPACT,  
173 and OsloCTM3. The experiment required all participating models to (1) conduct three-year-  
174 simulations of 2016-2018 (i.e., covering the whole ATom observation period); (2) use or nudge  
175 meteorological data for the simulation period; and (3) use the same pre-defined emission fields  
176 for precursor gases and aerosol tracers. The suggested emissions are the Coupled Model  
177 Intercomparison Project Phase 6 (CMIP6) (Feng et al., 2020) for anthropogenic source, daily  
178 biomass burning emission (such as The Global Fire Assimilation System (GFAS)), a dataset  
179 based on satellite volcanic SO<sub>2</sub> observations from the OMI instrument on the Aura satellite (Carn  
180 et al., 2016, 2017) for outgassing and eruptive volcanic emission, and DMS concentration in sea  
181 surface from Lana et al. (2011). Wind-driven emissions, such as dust and sea salt, are calculated  
182 online by each model. Following the experimental protocol, all models provided results for all  
183 AToms except for OsloCTM3 that omitted data in ATom-4. Unlike traditional AeroCom  
184 experiments that used gridded daily/monthly averaged data, modelers are required to interpolate  
185 model results along flight track every 10-s (see more discussion in Sect. 3.1) using three-  
186 dimensional high frequency (e.g., hourly or even less depending on the models' time step) data  
187 to facilitate the comparison. It is worth noting that the models do not have any actual information  
188 at 10-s time resolution, given their time steps are at least 10<sup>×</sup> greater and their spatial resolutions  
189 are coarse. However, the interpolation methodology suggested here provides the best model



190 information at their current configuration to compare with aircraft measurements. Table 2  
191 summarizes the detailed model characteristics and input datasets relevant to this study.

192  
193 The AeroCom-ATom experiment also designed three sensitivity simulations by tracking gas and  
194 aerosol emissions to anthropogenic, biomass burning, and volcanic sources to attribute the origin  
195 of sulfur sources on sulfur simulations over remote oceans. These experiments were conducted  
196 with the Goddard Earth Observing System (GEOS) model. The setup of the GEOS model  
197 followed the experiment protocol generally, but GEOS used its own daily biomass burning  
198 emissions that were derived from the Quick Fire Emissions Dataset (QFED) developed based on  
199 MODIS fire radiative power and calculated in near real-time at  $0.1^\circ$  resolution (Darmanov and  
200 da Silva, 2015; Pan et al., 2020). Emissions from biogenic sources were calculated using the  
201 Model for Emissions of Gases and Aerosols from Nature (MEGAN) embedded in the GEOS  
202 model.

### 203 204 **3. ATom-AeroCom comparisons of sulfur species**

205 This section presents a comparison of sulfur species between ATom measurements and  
206 AeroCom model simulations. The consistency and diversity of data across remote regimes, both  
207 horizontally and vertically, help us understand the effects of emissions, transport, and chemical  
208 transformations, and shed light on improving the processes in models to best represent the ATom  
209 observations.

#### 210 211 **3.1 Overall comparison**

212 The overall performance of  $\text{SO}_4$  PDF distribution observed from the AMS and PALMS  
213 instruments and simulated by five AeroCom models for four ATom deployments is presented in  
214 Fig. 2. Also shown in Fig. 2 are the corresponding various percentiles, namely, 0<sup>th</sup> (minimum),  
215 25<sup>th</sup>, 50<sup>th</sup> (median), 75<sup>th</sup>, and 100<sup>th</sup> (maximum), and the mean for statistical analyses. As  
216 mentioned in Sect. 2.1, we have AMS data at three sampling intervals (i.e., 1-s, 60-s, and 10-s).  
217 The 10-s merged dataset were deliberately provided by the ATom observation team for  
218 integrating data from various instruments to a unified temporal resolution. We intend to use this  
219 dataset for investigation on regional and seasonal bases. Before applying it, however, we first  
220 evaluate the quality of the 10-s data. Previous studies (Hodzic et al., 2020) indicated  
221 measurement precision improved with the square root of the number of sampling points. In other  
222 words, averaging data over a 60-s interval is better than averaging over 1-s or 10-s intervals  
223 because there are more sample points in a 60-s interval. This also applies to the detection limit  
224 (DL) as it is just 3 times the precision. DL flags are assigned to convey semi-quantitative  
225 information when sampling conditions are beyond the instrument detection range and the  
226 measurements are not quantifiable. Despite the differences, the three PDFs of AMS  $\text{SO}_4$  (red,  
227 using all relevant data including negatives) are nearly identical. Statistical analyses were further  
228 performed on the AMS 60-s, 10-s, and 1-s data sets by (1) all sampling points, even negative  
229 values, as indicated by the dot-dash box-and-whisker (approach 1), and (2) sampling points when  
230 their values exceeded DL as shown by solid box-and-whisker (approach 2). The  $\text{SO}_4$  median  
231 (and mean) values of 60-s are closer to 10-s' but lesser than 1-s' by 0-10% in approach 1. There  
232 is slightly greater diversity (~30%, solid box-and whisker) between these statistical values in  
233 approach 2, and the data in 60-s and 10-s are also relatively close, with a difference less than  
234 ~20%. These comparisons of the PDFs with noise and signal tell us that, on average,  $\text{SO}_4$  is high  
235 enough in the ATom background to be unaffected by noise at any resolution. A similar analysis



236 (not shown here) of SO<sub>2</sub> and DMS measurements also showed agreement between the 10-s  
237 interval dataset and the original dataset. Thus, the use of the 10-s data is acceptable in our study,  
238 given the significant differences in tracer statistics between model simulations and between  
239 model and observation.

240  
241 We use 10-s merged data where observations above DL throughout the main text unless  
242 otherwise stated. When multiple instruments measured the target field, only points where all  
243 instrument measured above DL values were included in analysis, as AMS 10-s in orange and  
244 PALMS 10-s in grey in Fig. 2. All model results were sampled mimicking flight observations  
245 (see Sect. 2.2), and only data with measurements available were used in comparison. This  
246 approach ensures that model evaluation is based on high-quality measurements. It is worth  
247 noting that the given statistical values in this method represent more regions having high tracer  
248 concentration or mixing ratio. In the supplementary material, we further give a model-  
249 observation comparison for all available measurement data including negatives. The observed  
250 and simulated PDF distributions are presented separately in Fig. 2.

251  
252 Most observed and simulated SO<sub>4</sub> exhibit highest probability density around SO<sub>4</sub> values of 10-  
253 100 ng sm<sup>-3</sup>. With the exception of GEOS and CAM-ATRAS, the model SO<sub>4</sub> PDFs show higher  
254 tails beyond 100 ng sm<sup>-3</sup>, which explain the higher median and mean SO<sub>4</sub> simulated by the  
255 models. Clearly, the diversity among model simulated SO<sub>4</sub> is high. Although the mean of  
256 PALMS SO<sub>4</sub> is generally about 10-50% higher than AMS SO<sub>4</sub>, this difference is much smaller  
257 than the difference between models that can easily exceed several orders of magnitude. The  
258 lower SO<sub>4</sub> of AMS than PALMS may be due at least in part to the fact that the sample size range  
259 of AMS (~0.75 μm) is smaller than that of PALMS (~3 μm), as mentioned in Sect. 2.1. In  
260 general, nearly all measurements and models indicate that SO<sub>4</sub> concentrations on a global ocean  
261 basis are lowest (or highest) during the Northern Hemisphere (NH) summer (or spring) season.  
262 Similar analysis was also performed on all (e.g., both positive and negative) measurement data  
263 (Fig. S1), the median/mean values of observations are naturally smaller than those in Fig. 2 by 8-  
264 20%, but the PDF distributions are almost identical between the two treatments.

265  
266 Figure 3 shows the PDF distribution and statistics for SO<sub>2</sub>. All observed and simulated data were  
267 reprocessed by including points above the detection limit (2 pptv) only. Both instruments (CIMS  
268 and LIF) were deployed during ATom-4. Despite CIMS being less precise than LIF (Rollins et  
269 al., 2016), both instruments agreed within 95% and CIMS measured SO<sub>2</sub> concentrations were  
270 consistently 3-7% lower than LIF measurements. This difference is within the combined  
271 uncertainties of the two measurements, but it suggests a systematic calibration error in one or  
272 both instruments that is currently unresolved (Rickly et al., 2021). Meanwhile, the width of  
273 CIMS SO<sub>2</sub> PDF (measured at half-height) is narrower in ATom-4, with peak heights around 10  
274 pptv and is more consistent with LIF measurements and model simulations. In contrast, the  
275 distribution of SO<sub>2</sub> measured by CIMS during ATom-1 to -3 is spread much wider than the  
276 models. This wider distribution needs to be examined given the degree of seasonal variation in  
277 the SO<sub>2</sub> PDF. CIMS adjusted its CToF between ATom-3 and -4 to improve resolution, and  
278 thereafter managed to fit SO<sub>2</sub> and formate-H<sub>2</sub>O independently, which was practically impossible  
279 for ATom-1 to -3. Throughout ATom periods, models, especially E3SM, GEOS, and  
280 OsloCTM3, show higher peak heights and narrower peak widths. Statistics indicate lower model  
281 SO<sub>2</sub> medians and higher simulated mean/median ratios than those of observations (see



282 corresponding values given in the figure). The model-observation agreement is much better in  
283 ATom-4 among the four ATom deployments. Figure S2 presents the corresponding analysis,  
284 including the measured negative values. Compared to Fig. 3, the observed median and mean  
285 values drop substantially (up to 50%), but the model statistics change relatively small.

286  
287 Atmospheric DMS observations are scarce, especially on a global scale. Thus, DMS  
288 measurements by the two instruments (WAS and TOGA) during the four ATom deployments  
289 provide an unprecedented opportunity to investigate biological DMS over global remote oceans  
290 and evaluate model DMS simulations on spatial and temporal distributions. By excluding points  
291 with measured values below detection limit (i.e., 1 pptv), the overall DMS comparison in Fig. 4  
292 indicates TOGA has higher data peaks and probability densities when DMS ranges from 3-10  
293 pptv. However, this does not appear to be consistent with the lower median and mean values of  
294 TOGA, indicating a higher tail in the WAS DMS PDF. Likewise, although the peak of WAS  
295 DMS PDF is significantly higher than all models from 3-10 pptv (~5-20 pptv for ATom-3), the  
296 median and mean of the WAS DMS are lower, suggesting an even higher tail in model DMS  
297 PDF. Overall, there is a big gap between the WAS and TOGA DMS measurements, and both are  
298 surprisingly low compared to the models. Statistical analysis performed on selected percentiles  
299 indicates that multi-model DMS medians are about 4.9 (ATom-1), 8.6 (ATom-2), 6.6 (ATom-3),  
300 and 7.7 (ATom-4) times higher than observed, while model GEOS has a better performance (i.e.,  
301 1.2, 2.7, 2.3, and 2.8 correspondingly). Even though the model DMS median is mostly higher  
302 than the observed value, the degree of overestimation is not as serious as the mean value that can  
303 be more than tenfold, indicating a few points are simulated with extraordinarily high DMS  
304 values. Based on what we know about DMS sources and sinks, these very large simulated DMS  
305 appear most commonly in the boundary layer (BL). Indeed it is confirmed in Fig 4c,f,i,l by  
306 looking at the ratios of DMS median values between model simulations and observations. The  
307 analyses are performed on four vertical ranges (e.g., the entire vertical column, the BL 0-1.5 km,  
308 the low-middle free troposphere 1.5-6 km, and the upper troposphere 6-12 km). The last column  
309 “MMM/MOM” refers to multi-model median to multi-observation median. Apparently, the high  
310 ratio stems mostly from the BL, above which the consistency is much better. Meanwhile, the  
311 PDF distribution and statistics of the models agree better with the WAS measurement than with  
312 the TOGA measurement. We should also acknowledge that this is a very limited set of  
313 observations we used here, and that there are some longer-term DMS observations near the  
314 surface that were used as input for the parameterization of DMS emissions. More DMS  
315 observations near the ocean surface are needed to make a confident comparison.

316  
317 DMS measurement is uniquely having a fraction of measured values in “-888”. An instrument  
318 typically has an operational detection range, which is defined by the lower limit of detection  
319 (LDL) and upper limit of detection (UDL). The flag for measured value less than the LDL is “-  
320 888” for TOGA and WAS data used in this study. The number of “-888” is not meaningless. It  
321 means that we know the value of a given measurement is below a known quantity, but we are not  
322 able to quantify that value precisely. Fig. S3 shows a similar DMS PDF analysis as Fig. 4, but  
323 instead of excluding the “-888” measurements, these are replaced with “0” as suggested by the  
324 instrument PIs. The percentage (P) of the measured “-888” is given for TOGA and WAS  
325 measurement data in the figure. These Ps for all AToms range 65% - 91%, which means majority  
326 of measured values are below LDL and the medians of both TOGA and WAS data are zero.  
327 Correspondingly, the multi-model average median (0.22, 1.13, 1.10, and 1.34 pptv for ATom-1



328 to -4 respectively) are much lower than those in Fig. 4. The ratio of means between model and  
329 observation for all AToms is 9.1 in Fig. S3, which is ~44% higher than 6.3 in Fig. 4.

330

331

### 3.2 Vertical profiles

332

333

334

335

336

337

338

339

Vertical profiles of ATom-1 to -4 for observed and modeled SO<sub>4</sub>, SO<sub>2</sub>, DMS, and MSA are shown in Figs. 5-8, respectively, for five latitude bands (from the north to the south) and for both the Pacific and Atlantic Ocean basins. Again, the profiles include equal amounts of data for each measurement and model result. In other words, all comparisons show only available points where the two observed values (i.e., AMS vs. PALMS for SO<sub>4</sub> and MSA, CIMS vs. LIF for SO<sub>2</sub>, and TOGA vs. WAS for DMS) are greater than their detection limits, and where the model values are extracted.

340

341

342

343

344

345

346

347

348

349

350

351

352

353

354

355

The average and range of sulfur tracers for ATom-1 to -4 are shown in Figs. 5-8 and their corresponding details in each ATom are further given in Figs. S4-7. As shown in Fig. 5, the SO<sub>4</sub> measured by the two instruments are close to each other and lie generally within the span of modelled SO<sub>4</sub> throughout the ATom periods. The spread of modeled SO<sub>4</sub> concentrations is large, easily exceeding an order of magnitude, especially in the upper troposphere. Despite that improvements are needed, the models are able to capture the shape of the SO<sub>4</sub> profile generally. These five models can generally be divided into three groups according to their SO<sub>4</sub> vertical profiles: 1. CAM-ATRAS and GEOS, 2. E3SM, and 3. IMPACT and OsloCTM. Over tropical and northern hemisphere oceans, Group 1 captures the SO<sub>4</sub> vertical profile well, while Group 3's vertical profile does not decrease enough at higher altitudes. The CAM-ATRAS model recently reported an improvement of aerosol wet scavenging processes, which allow efficient removal of aerosols by convective clouds and precipitation in the tropical and mid-latitude troposphere, while trace gases such as SO<sub>2</sub> to reach the upper troposphere (Liu and Matsui's 2021). In the free troposphere at high southern latitudes, SO<sub>4</sub> is too low for Group 1 and too high for Group 3. Group 2 (i.e., E3SM) has SO<sub>4</sub> simulations between the other two groups.

356

357

358

359

360

361

362

363

364

365

366

367

368

369

370

371

372

373

Figure 6 shows generally lower modeled SO<sub>2</sub> volume mixing ratios compared to the CIMS observations for most altitudes and latitude bins. The spread among modeled SO<sub>2</sub> values exceeds an order of magnitude, but around the measured SO<sub>2</sub>. SO<sub>2</sub> is better simulated by model IMPACT in the NH and by models CAM-ATRAS and OsloCTM3 in the Southern Hemisphere (SH). The tropical Pacific appears to be an interesting region where all models need to improve SO<sub>2</sub> simulations from the surface to 400mb. Basically, the observed SO<sub>2</sub> is high at the surface, falls rapidly in the BL, and then gradually decreases above the BL, except for ATom-1, during which a second peak appears just above the BL (see Fig. S5 for the details of ATom-1 to -4 separately). These observations indicate a strong local source for SO<sub>2</sub> in all seasons and a transport source in the low free-troposphere NH summer (ATom-1). Like observations, the model GEOS provides a local source for SO<sub>2</sub> at the surface, but it misses the plume above the BL in ATom-1, and its vertical SO<sub>2</sub> convection is consistently too weak. Since only one flight was in ATom-1, more observations are needed to confirm whether GEOS has been failing to catch the plume there during the NH summer. All other models miss the strong local source and simulate SO<sub>2</sub> transport in the low free-troposphere, which is only shown to a lesser extent in ATom-1 observation. Figure S5 also shows an excellent agreement of SO<sub>2</sub> profiles measured by the CIMS and LIF during ATom-4 and models agree with measurements better in ATom-4 as well. Modeled SO<sub>2</sub> volume mixing ratios are generally lower compared to the CIMS observations for most altitudes





374 and latitude bins in ATom-1 to -3, which may be partially owing to the CIMS measurement issue  
375 discussed in Sect. 3.1.

376  
377 DMS measurements fill in another piece of the puzzle for the atmospheric sulfur budget. As  
378 shown in Fig. 7, all five AeroCom models generally overestimate DMS in the BL, particularly  
379 for models CAM-ATRAS and OsloCTM3. This large bias close to the surface requires us to  
380 revisit the DMS emissions employed in our models. In these five models, DMS emissions from  
381 CAM-ATRAS, E3SM, and IMPACT are directly derived from climate emissions inventories.  
382 GEOS calculates DMS emissions based on monthly climatological DMS concentrations in ocean  
383 water (Lana et al., 2011) and modeled sea surface wind and temperature. OsloCTM3 oceanic  
384 DMS is parameterized as in Nightingale et al. (2000). The parameterization converts the monthly  
385 DMS ocean concentration, which is taken from Kettle and Andreae (2000), a climatology based  
386 on observations, to a flux based on wind speed from the meteorological data. It is worth to note  
387 that even the latest climatological database by Lana et al., (2011) was constructed by compiling  
388 measurements before 2000, so the potential long-term change of DMS emission caused by  
389 environment change could be missed (Barford, 2013). Also, although the data used by Lana et al.  
390 (2011) is large (i.e., ~47,000 seawater concentration measurements), interpolation and  
391 extrapolation techniques were still necessary in creating a global monthly climatological DMS  
392 emission. Gali et al. (2018) reported updated oceanic DMS levels on a global scale using remote  
393 sensing satellite data. However, much effort is still needed to accurately establish global rates of  
394 change in order to create global DMS emissions for climate modeling.

395  
396 Meanwhile, the modeled DMS vertical gradient is generally steeper than the observed one,  
397 implying slower vertical transport or faster chemical conversion of DMS to SO<sub>2</sub> in the model.  
398 The data collected from the AeroCom models did not provide us with enough information to  
399 tease out the determinants. Currently, GEOS and OsloCTM3 account for two products from the  
400 oxidation of DMS (i.e., SO<sub>2</sub> and MSA) but only GEOS output MSA results. The other models  
401 consider DMS oxidation products only as SO<sub>2</sub>. These chemical processes in the model may also  
402 need to be revisited. Previous studies proposed other chemical reactions for DMS loss in the  
403 atmosphere. For example, halogen chemistry represented 71% of the DMS loss in the study of  
404 Hoffmann et al., (2016). Veres et al. (2020) estimated that about 30% of DMS in the atmosphere  
405 was oxidized to a sulfur compound, hydroperoxymethyl thioformate (HPMTF), reported only in  
406 ATom-4. To this end, the HPMTF serves as a new reservoir of oceanic sulfur and its life cycle in  
407 the atmosphere is unknown. The new finding indicates that important components of Earth's  
408 sulfur cycle are not yet been fully understood and urges us to reassess this fundamental marine  
409 chemical cycle. However, including these chemical DMS losses further reduces DMS above the  
410 surface, making DMS in the models even lower at high altitudes.

411  
412 Of the five models, only GEOS reports MSA (Fig. 8). The GEOS MSA matches observations in  
413 the lower troposphere. In the upper troposphere (UT), the GEOS MSA tends to decrease slowly  
414 or even increase with altitude. These behaviors are inconsistent with observations, and this  
415 inconsistency can be explained at least partially by the MSA phase stages defined in the model  
416 and observations. AMS and PALMS only measure the particle phase of MSA, but GEOS MSA  
417 is the total MSA and is not accurately represented by observations, especially in UT. Yan et al.  
418 (2019) reported that the ratio of MSA to SO<sub>4</sub> can be reduced by 30% when calculations do not  
419 consider methanesulfonic acid in the gas phase (MSAg) at low temperatures.



420

421

### 3.3 Regional and seasonal analysis

422

Further analyses on regional and seasonal basis are given in Figs 9-11 for SO<sub>4</sub>, SO<sub>2</sub>, and DMS, respectively. Only multi-model median is shown here to highlight any common problems in the models. Further details of each individual model are given in Figs. S8-10 and discussed in supplementary material. Each model in this study has its anomalous behavior at a specific time and location. With this knowledge, modelers can further explore the simulation to identify potential causes of model anomalies.

423

424

425

426

427

428

429

High SO<sub>4</sub> concentration regions vary across seasons (Fig. 9). In free-troposphere, these regions cover the tropics to mid-latitudes in summer and winter (i.e., ATom-1 and ATom-2) and shift to mid- to high-latitudes in spring and autumn (i.e., ATom-3 and ATom-4). The most high concentration areas appeared in the SH high-latitudes during ATom-3 (SH spring) and the NH high-latitudes during ATom-4 (NH spring). Things are a bit more complicated in the BL, but the tropical atmospheric SO<sub>4</sub> concentration appears to be always elevated, and SO<sub>4</sub> concentration levels and SO<sub>4</sub> interregional variation are more pronounced in ATom-1 (NH summer). Among all AToms, the performance of the model SO<sub>4</sub> simulation is best for ATom-4 and worst for ATom-1 (NH summer). Compared to observation, the free tropospheric atmosphere simulated by the models tends to be more polluted. SO<sub>4</sub> concentration levels in simulated and observed worlds can differ significantly in certain areas of each ATom. Differences may be caused by majority models or a few individual models, and more discussion is given in the Supplement.

430

431

432

433

434

435

436

437

438

439

440

441

442

Atmospheric SO<sub>2</sub> (Fig. 10) is most abundant in the BL of NH mid-latitude Pacific Ocean during ATom-1 (NH summer) and the tropical Pacific BL during ATom-3 (NH autumn), and pollution affects the atmosphere above. Areas where free tropospheric SO<sub>2</sub> pollution is relatively polluted do not necessarily follow the example of the BL. For instance, the SH mid-latitude Atlantic free troposphere appears to be more polluted than other regions in ATom-4, but not in the BL, implying a potential source of horizontal transport. The interregional variation of SO<sub>2</sub> in BL is much larger than in the free troposphere, from which local oceanic sources of SO<sub>2</sub> can be inferred. In terms of model-observation comparison, model simulated SO<sub>2</sub> in the free troposphere is generally lower, which is opposite to the case of SO<sub>4</sub>. A rapid SO<sub>2</sub> to SO<sub>4</sub> chemical conversion in models could be one of reasons.

443

444

445

446

447

448

449

450

451

452

453

454

455

456

457

458

459

460

461

462

463

Surface DMS (Fig. 11) is generally higher in the tropics when the ocean is warm and in mid-high latitudes when the hemisphere is in spring (e.g., ATom-3 SH spring and ATom-4 NH spring). A remarkable pattern of high model DMS values in the BL is revealed throughout the ATom cycle. This phenomenon also occurs in the free lower troposphere, but not necessarily in the upper troposphere, suggesting a potential slower vertical transport or faster DMS chemical loss in models. The high model DMS in BL can be attributed to (1) too high DMS emission, (2) too slow DMS chemical loss, and (3) too slow DMS vertical transport from BL to free troposphere. The convoluted effort can be somehow alleviated by focusing on remote high-latitudes, for example SH high-latitude (40S-70S) Pacific, where land source impacts are limited. Thus, the higher simulated SO<sub>2</sub> there in the BL ruled out a chemical cause due to low DMS loss. The extremely high surface DMS is also not due to the slow vertical transport giving simulated DMS is also high in the layers above the BL. A large model DMS emission is likely responsible for the simulated high surface DMS.



466

#### 467 **4 Sulfur budget from AeroCom models**

468 Table 3 summarizes the global sulfur budgets for emissions, wet/dry deposition and chemistry  
469 from the five models. Clearly, the largest source of sulfur (~70 TgS/yr) is SO<sub>2</sub> emitted directly  
470 from anthropogenic (~78%), biomass burning (~2%), and volcanic sources (~20%). Biogenic  
471 DMS (~15-30 TgS) produced and outgassed from decomposition of marine organic molecules  
472 provides the largest natural source of sulfur to the atmosphere. A small amount of SO<sub>4</sub> (< 3%) is  
473 emitted directly from anthropogenic sources.

474

475 DMS is oxidized in the atmosphere by OH and NO<sub>3</sub> radicals to form SO<sub>2</sub> and MSA. This  
476 biological source of SO<sub>2</sub>, along with SO<sub>2</sub> emitted directly from other sources, reacts with  
477 hydroxyl radicals (OH) in the gas phase and hydrogen peroxide (H<sub>2</sub>O<sub>2</sub>) and ozone (O<sub>3</sub>) in the  
478 aqueous phase to produce sulfuric acid (H<sub>2</sub>SO<sub>4</sub>) and eventually sulfate particles, which play an  
479 important role in the formation of clouds over the oceans.

480

481 In the five models, DMS has the shortest global average lifetime (0.6-2.0 days), followed by SO<sub>2</sub>  
482 (1.1-1.8 days), and SO<sub>4</sub> the longest lifetime (3.1-5.6 days). Among them, GEOS has the lowest  
483 global burden and shortest lifetime for all sulfur species. The magnitudes of global burdens and  
484 lifetimes shown here support the model performance shown in Figs. 2-8. For example, models  
485 CAM-ATRAS and OsloCTM3 emit highest DMS, which is consistent with the highest DMS  
486 value (Fig. 4 and S10) and longest lifetime simulated by the two models.

487

488 The key budget items include DMS emission, SO<sub>2</sub> emission, sulfate source or total deposition  
489 (source and deposition are pretty much the same as they should be), lifetime (reversely  
490 proportional to the loss rate), and total atmospheric mass load. From the multi-model mean and  
491 standard deviation, the “diversity” can be calculated. Figure 12 shows the global mean budget  
492 items in the percentage deviation of each model from the multi-model mean, following the same  
493 concept shown in Schulz et al., 2006 and Gliss et al., 2021. It reveals the processes causing  
494 model differences. For example, E3SM and GEOS have approximately the same SO<sub>2</sub> emissions  
495 and total sulfate sources, but the sulfate lifetime is much shorter in GEOS (implying faster  
496 removal rates) thus smaller sulfate burden that is consistent with lower sulfate concentrations in  
497 GEOS than in E3SM. At the same time, the lower total sulfate source in E3SM is compensated  
498 by longer lifetime compared to CAM-ATRAS, resulting in a comparable global burden of SO<sub>4</sub> in  
499 the two models.

500

501 It is worth pointing out that the much lower atmospheric SO<sub>4</sub> mass loading of the GEOS  
502 simulations is not necessarily related to the poor performance of the GEOS SO<sub>4</sub> simulations, as  
503 revealed by the model-measurement comparison in Figs 2, 5 and S8. Although the multi-model  
504 mean (or median) often represents the best simulation in the modeling domain, common  
505 modeling problems or too small model sample can compromise this effort.

506

#### 507 **5. Source origins for aerosol SO<sub>4</sub> along flight track and Ocean basins**

508 In this section, we perform an analysis of source attribution by tagging the sulfur source types  
509 using the GEOS model. This model is the only one that provides tagged data. Our goal is to  
510 understand the sources (anthropogenic, biological, volcanic) of sulfate aerosols in remote regions



511 and how chemistry, transport, and removal processes determine the vertical distribution of  
512 sulfate aerosols across seasons and ocean locations.

513  
514 Figure 13a presents a quantitative summary of the source attribution of aerosol SO<sub>4</sub> sampled  
515 along the ATom flight tracks. The analysis was performed over four seasons, spanning the  
516 troposphere and three vertical layers (i.e., marine boundary layer, free troposphere and upper  
517 troposphere). Overall, anthropogenic emissions were the dominant source (40–60% of the total)  
518 of simulated tropospheric SO<sub>4</sub> along the ATom flight tracks for almost all altitudes and seasons,  
519 followed by volcanic (18–32%) and oceanic sources (16–32%). Anthropogenic pollution  
520 prevailed over remote oceans most in spring and autumn (ATom-3 and -4). The overall  
521 contributions from volcanic and oceanic sources are comparable during the ATom periods.  
522 Meanwhile, the ocean source contribution has an obvious seasonal variation which is most active  
523 during the SH summer (ATom-2), when marine biochemical activity in the vast Southern Ocean  
524 is at its most active. Volcanos show the largest contribution in the NH summer 2016 (ATom-1)  
525 during the four ATom deployments. Given the irregular and event character of eruptions, the  
526 volcanic contribution deserves further discussion below.

527  
528 In the vertical direction, SO<sub>4</sub> from anthropogenic emissions contributes more than 50% to the  
529 free to upper troposphere. Even in the marine boundary layer, anthropogenic sources of SO<sub>4</sub> still  
530 account for the largest fraction, except in the SH summer (ATom-2) where and when oceanic  
531 source became dominant. The relative importance of volcanic and marine sources varies not only  
532 seasonally but also vertically. Oceanic sources understandably make up a significant fraction  
533 (26–42%) of SO<sub>4</sub> in the boundary layer. In the free troposphere, its contribution drops off  
534 sharply, reflecting its local surface source characteristics. On the other hand, SO<sub>4</sub> from  
535 anthropogenic emissions expands in the free troposphere, suggesting that the source originated  
536 from distant continental areas. Volcanic SO<sub>4</sub> remains nearly constant throughout the troposphere,  
537 making volcanoes the second largest source there. Meanwhile, the contribution of biomass  
538 burning to SO<sub>4</sub> over remote oceans is relatively small (< 3%).

539  
540 The sources of SO<sub>4</sub> discussed above are deduced from the location and timing of the ATom's  
541 flight path. Conclusions about the total contribution of the ocean needs caution, as there may be  
542 representativeness issues using such narrow-band and instantaneous sampling. There might be a  
543 situation where, for example, volcanoes provide a very large signal but only account for a small  
544 measured area, and in most regions, volcanoes play a very minor role. Whereas oceanic sources  
545 in the marine boundary layer perhaps were the dominant source for a much wider region but the  
546 SO<sub>4</sub> concentration resulting from the DMS was overall a smaller amount compared to other  
547 sources where near a volcanic or anthropogenic source. To address this representation issue, we  
548 perform one more analysis with the model data averaged over a wider oceanic region (the shaded  
549 orchid area in Fig. 1) and over a longer period (i.e., monthly mean over ATom periods). Such  
550 source attributions are given in Fig. 13b.

551  
552 Qualitative conclusions drawn from source attribution along the flight tracks generally apply to  
553 the ocean basin source attribution, albeit to a slightly different extent. This confirms that  
554 continental man-made sources dominate tropospheric SO<sub>4</sub> even over oceans. It has a clear  
555 seasonal variation in oceanic contribution, which is largest in austral summer (ATom-2)  
556 followed by boreal summer (ATom-1). There are two types of volcanic emissions. Volcanic



557 degassing emissions tend to remain nearly constant throughout the year and are equivalent to  
558 about 20% of SO<sub>2</sub> global anthropogenic emissions. This degassing emission ensures that  
559 volcanoes contribute more than 20% to SO<sub>4</sub> over the oceans. Due to the irregularity of volcanic  
560 eruptions in terms of different eruption locations, magnitudes, and times, explosive volcanic  
561 eruptions can cause severe fluctuations in SO<sub>4</sub> in the atmosphere. Compared with the source  
562 attribution along the flight trajectory, the volcanic contribution decreased over a larger spatial  
563 and temporal domain (i.e., ocean basin and monthly mean) in the NH winter 2017 by 32%  
564 (ATom-2) and increased in all other three seasons by 14-33%, especially in the NH spring 2018  
565 (ATom-4), when the massive Kilauea eruption in Hawaii began on 3 May 2018. Contrarily, the  
566 anthropogenic contribution increased in the NH winter (ATom-2) by 5% and decreased in other  
567 seasons by 7-21%.

568

## 569 **6. Conclusions**

570 This study investigates sulfur in remote tropospheric regions at global and seasonal scales using  
571 ATom measurements and AeroCom models. The goal is to understand the atmospheric sulfur  
572 cycle over the remote oceans, each model's behavior and the spread of model simulations, as  
573 well as the observation-model discrepancies. Such understanding and comparison with real  
574 observations are crucial to narrow down the uncertainty in model sulfur simulation. Even after  
575 decades of development, models are still struggling to accurately simulate sulfur distributions,  
576 with differences between models often exceeding an order of magnitude. On the other hand, the  
577 agreement between instruments is usually much better. Differences between modeled SO<sub>4</sub> are  
578 particularly large in the tropical upper troposphere, where deep convective transport allows a  
579 small portion of sulfur sources to reach the lower stratosphere where resultant sulfate aerosols  
580 can persist for many years. Compared with observations, simulated SO<sub>2</sub> is generally low while  
581 SO<sub>4</sub> is high, and the model-observation agreement is much better in ATom-4. Modeled DMS  
582 values are typically an order of magnitude higher than observed DMS near the surface, pointing  
583 to a need to revisit the DMS emission inventories and/or the biogeochemical modules used to  
584 predict DMS emissions. Our work also suggests investigating three other potential corresponding  
585 processes: whether the chemical conversion from SO<sub>2</sub> to SO<sub>4</sub> is too rapid, whether DMS-  
586 generated free tropospheric SO<sub>2</sub> is too low, and whether the vertical transport of SO<sub>2</sub> from BL to  
587 free troposphere is too low. This further investigation requires atmospheric oxidant fields and the  
588 ability to track SO<sub>2</sub> production and loss using tagged tracers.

589

590 We investigate source attribution of SO<sub>4</sub> over remote oceans seasonally and vertically. Sampled  
591 at the location and time of ATom measurements, anthropogenic emissions were the dominant  
592 source (40–60% of the total) of simulated tropospheric SO<sub>4</sub> at almost all heights and seasons,  
593 followed by volcanic (18–32%) and oceanic sources (16 – 32%). These contributions changed to  
594 34-56%, 17-37%, and 19-37% when extended to the broad Pacific and Atlantic during the  
595 months of ATom deployment. This survey confirms that anthropogenic sources from land  
596 dominate tropospheric SO<sub>4</sub> even over oceans. Given that we find DMS source to be  
597 overestimated in the models, the anthropogenic sources overall are a larger portion of the budget,  
598 and biogenic is likely smaller than volcanic. Volcanic degassing throughout the year contributes  
599 about 20%, and this proportion is increased by explosive eruptions that vary in location and  
600 timing. The oceanic contribution has obvious seasonal variation, the largest in the Southern  
601 Hemisphere summer, followed by the Northern Hemisphere summer.

602



603 It is understood that anthropogenic sulfur emissions currently offset a significant portion of  
604 greenhouse gas warming, but they are rapidly declining through emissions controls. As these  
605 anthropogenic emissions decrease, natural sources of sulfur, particularly bio-derived sulfur  
606 compounds discharged from the world's oceans, will increase their relative contribution.  
607 Therefore, more efforts are needed to understand the sulfur cycle in remote environments. On the  
608 other hand, our study shows that anthropogenic emissions remain a major source of sulfate  
609 aerosols generated over remote oceans during the ATom deployment periods, suggesting that  
610 any limitation of anthropogenic sulfur emissions would have modern global implications.

611  
612 *Code availability.* The GEOS Earth System Model source code and the instructions for model build are available  
613 at <https://github.com/GEOS-ESM/GEOSgcm/> (Last accessed: 28 August 2023).

614  
615 *Data availability.* The AeroCom model outputs needed to reproduce the results described in this paper are  
616 publicly available for download at <https://acd-ext.gsfc.nasa.gov/anonftp/acd/tropo/bian/ATom-AeroCom-Sulfur/>.  
617 The ATom data was obtained from their ESPO Data Archive: <https://espo.nasa.gov/atom/content/ATom>, last  
618 accessed: 28 August 2022.

#### 619 *Author contributions.*

620 BH and MC conceptualized ATom-AeroCom experiment. BH performed analysis and wrote the manuscript. BH,  
621 PRC, MLi, MTL, RBS, HM, JEP, HW, KZ, and JZ provided AeroCom model results and ECA, KF, RSH, JJ, PCJ,  
622 MLa, BAN, AWR, GS, and LX contributed to ATom measurements. All authors contributed to the editing of the  
623 manuscript.

#### 624 *Competing interests.*

625  
626 At least one of the co-authors is a member of the editorial board of Atmospheric Chemistry and Physics.

#### 627 *Acknowledgements.*

628  
629 HB, MC, and PRC acknowledge the GEOS model developmental efforts at Global Modeling and Assimilation  
630 Office (GMAO). This work was supported by NASA's Aura STM and ISFM programs and ACMAP award  
631 (80NSSC23K1000). The computing resources supporting this work were provided by the NASA High-End  
632 Computing (HEC) Program through the NASA Center for Climate Simulation (NCCS).  
633 ECA and RSH acknowledge the support of the National Center for Atmospheric Research, which is a major facility  
634 sponsored by the National Science Foundation under Cooperative Agreement No. 1852977.  
635 ML acknowledges the support of JSPS Postdoctoral Fellowships for Research in Japan (Standard).  
636 HM was supported by the Ministry of Education, Culture, Sports, Science, and Technology and the Japan Society  
637 for the Promotion of Science (MEXT/JSPS) KAKENHI grants (JP19H05699, JP19KK0265, JP20H00196,  
638 JP20H00638, JP22H03722, JP22F22092, JP23H00515, and JP23H00523); by the MEXT Arctic Challenge for  
639 Sustainability II (ArCS II) project (JPMXD1420318865); and by the Environment Research and Technology  
640 Development Fund 2-2003 (JPMEERF20202003) and 2-2301 (JPMEERF20232001) of the Environmental  
641 Restoration and Conservation Agency.  
642 KZ and HW acknowledge support by the U.S. Department of Energy (DOE), Office of Science, Office of Biological  
643 and Environmental Research, Earth and Environmental Systems Modeling program. The Pacific Northwest National  
644 Laboratory (PNNL) is operated for DOE by Battelle Memorial Institute under contract DE-AC05-76RLO1830.  
645 LX thanks Michelle Kim, Hannah Allen, John Crouse, and Paul Wennberg for operating the CIT CIMS instrument  
646 during ATom. LX acknowledges NASA grant NNX15AG61A.  
647 MTL thanks Marit Sandstad (CICERO) for assistance with the model post-processing and acknowledges  
648 the National Infrastructure for High Performance Computing and Data Storage in Norway (UNINETT) resources  
649 (grant NN9188K).  
650 RBS acknowledges funding from the Research Council of Norway (grant number 314997).

#### 651 **References**



- 654 Abdul-Razzak, H. and Ghan, S.: A parameterization of aerosol activation, 2. Multiple aerosol  
655 types, *J. Geophys. Res. Atmos.*, 105, 6837–6844, <https://doi.org/10.1029/1999JD901161>, 2000.
- 656 Allen, H. M., Bates, K. H., Crouse, J. D., Kim, M. J., Teng, A. P., Ray, E. A., and Wennberg,  
657 P. O.: H<sub>2</sub>O<sub>2</sub> and CH<sub>3</sub>OOH (MHP) in the Remote Atmosphere: 2. Physical and Chemical  
658 Controls, *J. Geophys. Res. Atmos.*, 127, e2021JD035702,  
659 <https://doi.org/10.1029/2021JD035702>, 2022.
- 660 Bacmeister, J., Suarez, M., and Robertson, F. R.: Rain Reevaporation, Boundary-Layer,  
661 Convection Interactions, and Pacific Rainfall Patterns in an AGCM, *J. Atmos. Sci.*, 63, 3383–  
662 3403, <https://doi.org/10.1175/JAS3791.1>, 2006.  
663
- 664 Barahona, D. and Nenes, A.: Parameterizing the competition between homogeneous and  
665 heterogeneous freezing in cirrus cloud formation – monodisperse ice nuclei, *Atmos. Chem.*  
666 *Phys.*, 9, 369–381, <https://doi.org/10.5194/acp-9-369-2009>, 2009.  
667
- 668 Barahona, D., Molod, A., Bacmeister, J., Nenes, A., Gettelman, A., Morrison, H., Phillips, V.,  
669 and Eichmann, A.: Development of two-moment cloud microphysics for liquid and ice within  
670 the NASA Goddard Earth Observing System Model (GEOS-5), *Geosci. Model Dev.*, 7, 1733–  
671 1766, <https://doi.org/10.5194/gmd-7-1733-2014>, 2014.  
672
- 673 Barford, E.: Rising ocean acidity will exacerbate global warming, *Nature*,  
674 <https://doi.org/10.1038/nature.2013.13602>, 2013.  
675
- 676 Bian, H., Luo, C., and Li, X.: Numerical modeling of air pollutant and rainfall effect on acid wet  
677 deposition, *ACTA Meteorol. Sin.*, 7, 3, 273–286, 1993.  
678
- 679 Bian, H., Chin, M., Hauglustaine, D. A., Schulz, M., Myhre, G., Bauer, S. E., Lund, M. T.,  
680 Karydis, V. A., Kucsera, T. L., Pan, X., Pozzer, A., Skeie, R. B., Steenrod, S. D., Sudo, K.,  
681 Tsigaridis, K., Tsimpidi, A. P., and Tsyro, S. G.: Investigation of global nitrate from the  
682 AeroCom Phase III experiment, *Atmos. Chem. Phys.*, 17, 12911–12940,  
683 <https://doi.org/10.5194/acp-17-12911-2017>, 2017.  
684
- 685 Boucher, O., Randall, D., Artaxo, P., Bretherton, C., Feingold, G., Forster, P., Kerminen, V.-M.,  
686 Kondo, Y., Liao, H., Lohmann, U., Rasch, P., Satheesh, S., Sherwood, S., Stevens, B., and  
687 Zhang, X.: in: *Climate Change 2013: The Physical Science Basis*, in: *Contribution of Working*  
688 *Group I to the Fifth Assessment Report of the Intergovernmental Panel on Climate Change:*  
689 *Clouds and Aerosols*, edited by: Stocker, T., Qin, D., Plattner, G.-K., Tignor, M., Allen, S.,  
690 Boschung, J., Nauels, A., Xia, Y., Bex, V., and Midgley, P., Cambridge University Press,  
691 Cambridge, UK and New York, NY, USA, 571–657, 2013.  
692
- 693 Breen, K. H., Barahona, D., Yuan, T., Bian, H., and James, S. C.: Effect of volcanic emissions on  
694 clouds during the 2008 and 2018, *Atmos. Chem. Phys.*, 21, 7749–7771,  
695 <https://doi.org/10.5194/acp-21-7749-2021>, 2021.  
696



- 697 Brock, C. A., Williamson, C., Kupc, A., Froyd, K. D., Erdesz, F., Wagner, N., Richardson, M.,  
698 Schwarz, J. P., Gao, R.-S., Katich, J. M., Campuzano-Jost, P., Nault, B. A., Schroder, J. C.,  
699 Jimenez, J. L., Weinzierl, B., Dollner, M., Bui, T., and Murphy, D. M.: Aerosol size distributions  
700 during the Atmospheric Tomography Mission (ATom): methods, uncertainties, and data  
701 products, *Atmos. Meas. Tech.*, 12, 3081–3099, 2019.  
702
- 703 Carn, S. A., Clarisse, L., and Prata, A. J.: Multi-decadal satellite measurements of global  
704 volcanic degassing, *J. Volcanol. Geotherm. Res.*, 311, 99–134,  
705 <http://dx.doi.org/10.1016/j.jvolgeores.2016.01.002>, 2016.  
706
- 707 Carn, S. A., Fioletov, V. E., McLinden, C. A., and Krotkov, N. A.: A decade of global volcanic  
708 SO<sub>2</sub> emissions measured from space, *Sci. Rep.*, 7, 44095, <https://doi.org/10.1038/srep44095>,  
709 2017.  
710
- 711 Chin, M., Rood, R. B., Lin, S. J., Müller, J.-F., and Thompson, A. M.: Atmospheric sulfur cycle  
712 simulated in the global model GOCART: model description and global properties, *J. Geophys.*  
713 *Res. Atmos.*, 105, D20, 24671–24687, <https://doi.org/10.1029/2000JD900384>, 2000.  
714
- 715 Colarco, P. R., da Silva, A., Chin, M., and Diehl, T.: Online simulations of global aerosol  
716 distributions in the NASA GEOS-4 model and comparisons to satellite and ground-based aerosol  
717 optical depth, *J. Geophys. Res. Atmos.*, 115, D14207, <https://doi.org/10.1029/2009JD012820>,  
718 2010.  
719
- 720 Crouse, J. D., McKinney, K. A., Kwan, A., J. and Wennberg, P. O., Measurement of Gas-Phase  
721 Hydroperoxides by Chemical Ionization Mass Spectrometry, *Anal. Chem.*, 78, 19, 6726–6732,  
722 <https://doi.org/10.1021/ac0604235>, 2006.  
723
- 724 Darnenov, A. and da Silva, A.: The Quick Fire Emissions Dataset (QFED) - Documentation of  
725 versions 2.1, 2.2 and 2.4, NASA TM-2015-104606, Vol. 38, 183 pp., 2015.  
726
- 727 Dentener, F., et al. (2006). "Emissions of primary aerosol and precursor gases in the years 2000  
728 and 1750 prescribed data-sets for AeroCom." *Atmospheric Chemistry and Physics* 6: 4321-4344.  
729
- 730 Dong, X., Fu, J. S., Zhu, Q., Sun, J., Tan, J., Keating, T., Sekiya, T., Sudo, K., Emmons, L.,  
731 Tilmes, S., Jonson, J. E., Schulz, M., Bian, H., Chin, M., Davila, Y., Henze, D., Takemura, T.,  
732 Benedictow, A. M. K., and Huang, K.: Long-range transport impacts on surface aerosol  
733 concentrations and the contributions to haze events in China: an HTAP2 multi-model study,  
734 *Atmos. Chem. Phys.*, 18, 15581-15600, <https://doi.org/10.5194/acp-18-15581-2018>, 2018.  
735
- 736 Eger, P. G., Helleis, F., Schuster, G., Phillips, G. J., Lelieveld, J., and Crowley, J. N.: Chemical  
737 ionization quadrupole mass spectrometer with an electrical discharge ion source for atmospheric  
738 trace gas measurement, *Atmos. Meas. Tech.*, 12, 1935–1954, <https://doi.org/10.5194/amt-12-1935-2019>, 2019.  
739
- 740
- 741 Feng, L., Smith, S. J., Braun, C., Crippa, M., Gidden, M. J., Hoesly, R., Klimont, Z., van Marle,  
742 M., van den Berg, M., and van der Werf, G. R.: The generation of gridded emissions data for  
743 CMIP6, *Geosci. Model Dev.*, 13, 461–482, <https://doi.org/10.5194/gmd-13-461-2020>, 2020.





- 744  
745 Fountoukis, C. and Nenes, A.: Continued development of a cloud droplet formation  
746 parameterization for global climate models, *J. Geophys. Res. Atmos.*, 110, D11212,  
747 <https://doi.org/10.1029/2004JD005591>, 2005.
- 748  
749 Galí, M., Levasseur, M., Devred, E., Simó, R., and Babin, M.: Sea-surface dimethylsulfide  
750 (DMS) concentration from satellite data at global and regional scales, *Biogeosciences*, 15, 3497–  
751 3519, <https://doi.org/10.5194/bg-15-3497-2018>, 2018.
- 752  
753 Gliß, J., Mortier, A., Schulz, M., Andrews, E., Balkanski, Y., Bauer, S. E., Benedictow, A. M.  
754 K., Bian, H., Checa-Garcia, R., Chin, M., Ginoux, P., Griesfeller, J. J., Heckel, A., Kipling, Z.,  
755 Kirkevåg, A., Kokkola, H., Laj, P., Le Sager, P., Lund, M. T., Lund Myhre, C., Matsui, H.,  
756 Myhre, G., Neubauer, D., van Noije, T., North, P., Olivíe, D. J. L., Rémy, S., Sogacheva, L.,  
757 Takemura, T., Tsigaridis, K., and Tsyro, S. G.: AeroCom phase III multi-model evaluation of the  
758 aerosol life cycle and optical properties using ground- and space-based remote sensing as well as  
759 surface in situ observations, *Atmos. Chem. Phys.*, 21, 87–128, [https://doi.org/10.5194/acp-21-87-](https://doi.org/10.5194/acp-21-87-2021)  
760 2021, Jan., 2021.
- 761  
762 Grennfelt, P., Engleryd, A., Forsius, M., Hov, Ø., Rodhe, H., and Cowling, E.: Acid rain and air  
763 pollution: 50 years of progress in environmental science and policy, *Ambio*, 49, 849–864,  
764 <https://doi.org/10.1007/s13280-019-01244-4>, 2020.
- 765  
766 Gryspeerd, E., Povey, A. C., Grainger, R. G., Hasekamp, O., Hsu, N. C., Mulcahy, J. P., Sayer,  
767 A. M., and Sorooshian, A.: Uncertainty in aerosol-cloud radiative forcing is driven by clean  
768 conditions, *Atmos. Chem. Phys.*, 23, 4115–4122, <https://doi.org/10.5194/acp-23-4115-2023>,  
769 2023.
- 770  
771 Guo, H., Campuzano-Jost, P., Nault, B. A., Day, D. A., Schroder, J. C., Kim, D., Dibb, J. E.,  
772 Dollner, M., Weinzierl, B., and Jimenez, J. L.: The importance of size ranges in aerosol  
773 instrument intercomparisons: a case study for the Atmospheric Tomography Mission, *Atmos.*  
774 *Meas. Tech.*, 14, 3631–3655, 2021.
- 775  
776 Hodshire, A. L., Campuzano-Jost, P., Kodros, J. K., Croft, B., Nault, B. A., Schroder, J. C.,  
777 Jimenez, J. L., and Pierce, J. R.: The potential role of methanesulfonic acid (MSA) in aerosol  
778 formation and growth and the associated radiative forcings, *Atmos. Chem. Phys.*, 19, 3137–  
779 3160, 2019.
- 780  
781 Hodzic, A., Campuzano-Jost, P., Bian, H., Chin, M., Colarco, P. R., Day, D. A., Froyd, K. D.,  
782 Heinold, B., Jo, D. S., Katich, J. M., Kodros, J. K., Nault, B. A., Pierce, J. R., Ray, E., Schacht,  
783 J., Schill, G. P., Schroder, J. C., Schwarz, J. P., Sueper, D. T., Tegen, I., Tilmes, S., Tsigaridis,  
784 K., Yu, P., and Jimenez, J. L.: Characterization of organic aerosol across the global remote  
785 troposphere: a comparison of ATom measurements and global chemistry models, *Atmos. Chem.*  
786 *Phys.*, 20, 4607–4635, 2020.
- 787  
788 Hoffmann, E. H., Tilgner, A., Schrödner, R., Bräuer, P., Wolke, R. and Herrmann, H.: An  
789 advanced modeling study on the impacts and atmospheric implications of multiphase dimethyl



- 790 sulfide chemistry, *Proc. Natl. Acad. Sci. USA*, 113, 11776–11781,  
791 <https://doi.org/10.1073/pnas.1606320113>, 2016.  
792  
793 Holton, J. R., Haynes, P. H., McIntyre, M. E., Douglass, A. R., Rood, R. B., and Pfister, L.:  
794 Stratosphere-troposphere exchange, *Rev. Geophys.*, 33, 403–439,  
795 <https://doi.org/10.1029/95RG02097>, 1995.  
796  
797 Hoesly, R. M., Smith, S. J., Feng, L., Klimont, Z., Janssens-Maenhout, G., Pitkanen, T., et al.  
798 (2018). Historical (1750–2014) anthropogenic emissions of reactive gases and aerosols from the  
799 Community Emissions Data System (CEDS). *Geosci. Model Dev.*, 11,  
800 369–408. <https://doi.org/10.5194/gmd-11-369-2018>.  
801  
802 Huang, R.-J., Duan, J., Li, Y., Chen, Q., Chen, Y., Tang, M., Yang, L., Ni, H., Lin, C., Xu, W.,  
803 Liu, Y., Chen, C., Yan, Z., Ovadnevaite, J., Ceburnis, D., Dusek, U., Cao, J., Hoffmann, T., &  
804 O'Dowd, C. D., Effects of NH<sub>3</sub> and alkaline metals on the formation of particulate sulfate and  
805 nitrate in wintertime Beijing. *Sci. Total Environ.*, 717, 137190,  
806 <https://doi.org/10.1016/j.scitotenv.2020.137190>, 2020.  
807  
808 Huey, L. G., Tanner, D. J., Slusher, D. L., Dibb, J. E., Arimoto, R., Chen, G., Davis, D., Buhr,  
809 M. P., Nowak, J. B., Mauldin III, R. L., Eisele, F. L., and Kosciuch, E.: CIMS measurements of  
810 HNO<sub>3</sub> and SO<sub>2</sub> at the South Pole during ISCAT 2000, *Atmos. Environ.*, 38, 5411–5421,  
811 <https://doi.org/10.1016/j.atmosenv.2004.04.037>, 2004.  
812  
813 Jia, H., Ma, X., Yu, F., and Quaas, J.: Significant underestimation of radiative forcing by  
814 aerosol–cloud interactions derived from satellite-based methods, *Nat. Commun.*, 12,  
815 <https://doi.org/10.1038/s41467-021-23888-1>, 2021.  
816  
817 Jia, H., Quaas, J., Gryspeerdt, E., Böhm, C., and Sourdeval, O.: Addressing the difficulties in  
818 quantifying the Twomey effect for marine warm clouds from multi-sensor satellite observations  
819 and reanalysis, *Atmos. Chem. Phys.*, 22, 7353–7372, <https://doi.org/10.5194/acp-22-7353-2022>,  
820 2022.  
821  
822 Moch, J. M., Mickley, L. J., Keller, C. A., Bian, H., Lundgren, E. W., Zhai, S., and Jacob, D. J.:  
823 Aerosol-radiation interactions in China in winter: Competing effects of reduced shortwave  
824 radiation and cloud-snowfall-albedo feedbacks under rapidly changing emissions, *J. Geophys.*  
825 *Res. Atmos.*, 127, e2021JD035442, <https://doi.org/10.1029/2021JD035442>, 2022.  
826  
827 Josephson, D. C., Robinson, J. M., Chiotti, J., Jirka, K. J., and Kraft, C. E.: Chemical and  
828 biological recovery from acid deposition within the Honnedaga Lake watershed, New York,  
829 USA, *Environ. Monit. Assess.*, 186, 4391–4409, <https://doi.org/10.1007/s10661-014-3706-9>,  
830 2014.  
831  
832 Jurkat, T., Kaufmann, S., Voigt, C., Schäuble, D., Jeßberger, P., and Ziereis, H.: The airborne  
833 mass spectrometer AIMS – Part 2: Measurements of trace gases with stratospheric or tropo-  
834 spheric origin in the UTLS, *Atmos. Meas. Tech.*, 9, 1907–1923, [https://doi.org/10.5194/amt-9-](https://doi.org/10.5194/amt-9-1907-2016)  
835 1907-2016, 2016.



- 836  
837 Kettle, A. J. and Andreae, M. O.: Flux of dimethylsulfide from the oceans: A comparison of  
838 updated data sets and flux models, *J. Geophys. Res. Atmos.*, 105, 26793–26808,  
839 <https://doi.org/10.1029/2000JD900252>, 2000.  
840  
841 Klein, S. A., Zhang, Y., Zelinka, M. D., Pincus, R., Boyle, J., and Gleckler, P. J.: Are climate  
842 model simulations of clouds improving? An evaluation using the ISCCP simulator, *J. Geophys.*  
843 *Res. Atmos.*, 118, 1329–1342, <https://doi.org/10.1002/jgrd.50141>, 2013.  
844  
845 Lana, A., Bell, T. G., Simó, R., Vallina, S. M., Ballabrera-Poy, J., Kettle, A. J., Dachs, J., Bopp,  
846 L., Saltzman, E. S., Stefels, J., Johnson, J. E., and Liss, P. S.: An updated climatology of surface  
847 dimethylsulfide concentrations and emission fluxes in the global ocean, *Global Biogeochem.*  
848 *Cy.*, 25, GB1004, doi:10.1029/2010GB003850, 2011.  
849  
850 Liu, M. and Matsui, H.: Improved simulations of global black carbon distributions by modifying  
851 wet scavenging processes in convective and mixed-phase clouds, *J. Geophys. Res. Atmos.*, 126,  
852 e2020JD033890, <https://doi.org/10.1029/2020JD033890>, 2021.  
853  
854 Lund, M. T., Myhre, G., Haslerud, A. S., Skeie, R. B., Griesfeller, J., Platt, S. M., Kumar, R.,  
855 Myhre, C. L., and Schulz, M.: Concentrations and radiative forcing of anthropogenic aerosols  
856 from 1750 to 2014 simulated with the Oslo CTM3 and CEDS emission inventory, *Geosci. Model*  
857 *Dev.*, 11, 4909–4931, <https://doi.org/10.5194/gmd-11-4909-2018>, 2018.  
858  
859 Malavelle, F. F., Haywood, J. M., Jones, A., Gettelman, A., Clarisse, L., Bauduin, S., Allan, R.  
860 P., Karset, I. H. H., Kristjánsson, J. E., Oreopoulos, L., Cho, N., Lee, D., Bellouin, N., Boucher,  
861 O., Grosvenor, D. P., Carslaw, K. S., Dhomse, S., Mann, G. W., Schmidt, A., Coe, H., Hartley,  
862 M. E., Dalvi, M., Hill, A. A., Johnson, B. T., Johnson, C. E., Knight, J. R., O'Connor, F. M.,  
863 Partridge, D. G., Stier, P., Myhre, G., Platnick, S., Stephens, G. L., Takahashi, H., and  
864 Thordarson, T.: Strong constraints on aerosol–cloud interactions from volcanic eruptions,  
865 *Nature*, 546, 485–491, <https://doi.org/10.1038/nature22974>, 2017.  
866  
867 McDonnell, T. C., Driscoll, C. T., Sullivan, T. J., Burns, D. A., Baldigo, B. P., Shao, S., and  
868 Lawrence, G. B.: Regional target loads of atmospheric nitrogen and sulfur deposition for the  
869 protection of stream and watershed soil resources of the Adirondack Mountains, USA, *Environ.*  
870 *Pollut.*, 281, 117110, <https://doi.org/10.1016/j.envpol.2021.117110>, 2021.  
871  
872 Matsui, H.: Development of a global aerosol model using a two-dimensional sectional method: 1.  
873 Model design, *J. Adv. Model. Earth Syst.*, 9, 1921–1947,  
874 <https://doi.org/10.1002/2017MS000936>, 2017.  
875  
876 Matsui, H. and Mahowald, N.: Development of a global aerosol model using a two-dimensional  
877 sectional method: 2. Evaluation and sensitivity simulations, *J. Adv. Model. Earth Syst.*, 9, 1887–  
878 1920, <https://doi.org/10.1002/2017MS000937>, 2017.  
879  
880 Molod, A.: Constraints on the Total Water PDF in GCMs from AIRS and a High Resolution  
881 Model, *J. Climate*, 25, 8341–8352, <https://doi.org/10.1175/JCLI-D-11-00412.1>, 2012.



- 882  
883 Moorthi, S. and Suarez, M. J.: Relaxed Arakawa-Schubert. A parameterization of moist  
884 convection for general circulation models, *Mon. Weather Rev.*, 120, 978–1002,  
885 [https://doi.org/10.1175/1520-0493\(1992\)120<0978:RASAPO>2.0.CO;2](https://doi.org/10.1175/1520-0493(1992)120<0978:RASAPO>2.0.CO;2), 1992.  
886  
887 Myhre, G., Samset, B. H., Schulz, M., Balkanski, Y., Bauer, S., Bernsten, T. K., Bian, H.,  
888 Bellouin, N., Chin, M., Diehl, T., Easter, R. C., Feichter, J., Ghan, S. J., Hauglustaine, D.,  
889 Iversen, T., Kinne, S., Kirkevåg, A., Lamarque, J.-F., Lin, G., Liu, X., Lund, M. T., Luo, G., Ma,  
890 X., van Noije, T., Penner, J. E., Rasch, P. J., Ruiz, A., Seland, Ø., Skeie, R. B., Stier, P.,  
891 Takemura, T., Tsigaridis, K., Wang, P., Wang, Z., Xu, L., Yu, H., Yu, F., Yoon, J.-H., Zhang,  
892 K., Zhang, H., and Zhou, C.: Radiative forcing of the direct aerosol effect from AeroCom Phase  
893 II simulations, *Atmos. Chem. Phys.*, 13, 1853–1877, <https://doi.org/10.5194/acp-13-1853-2013>,  
894 2013.  
895  
896 Nightingale P. D., Malin G., Law C. S., Watson A. J., Liss P. S., Liddicoat M. I., et al. In  
897 situ evaluation of air-sea gas exchange parameterizations using novel conservative and volatile  
898 tracers. *Global Biogeochem. Cy.* 14, 373–387, <https://doi.org/10.1029/1999gb900091>, 2000.  
899  
900 Penner, A., Prather, J. E., Ramanathan, K. A., Ramaswamy, V., Rasch, V., Ravishankara, P. J.,  
901 Rosenfeld, A. R., Stephens, D., and Wood, R.: Improving our fundamental understanding of the  
902 role of aerosol–cloud interactions in the climate system, *P. Natl. Acad. Sci. USA*, 113, 5781–  
903 5790, <https://doi.org/10.1073/pnas.1514043113>, 2016.  
904  
905 Rasch, P. J., Xie, S., Ma, P. -L., Lin, W., Wang, H., Tang, Q., Burrows, S. M., Caldwell, P.,  
906 Zhang, K., Easter, R. C., Cameron-Smith, P., Singh, B., Wan, H., Golaz, J.-C., Harrop, B. E.,  
907 Roesler, E., Bacmeister, J., Larson, V. E., Evans, K. J., Qian, Y., Taylor, M., Leung, L. R.,  
908 Zhang, Y., Brent, L., Branstetter, M., Hannay, C., Mahajan, S., Mامتjanov, A., Neale, R.,  
909 Richter, J. H., Yoon, J.-H., Zender, C. S., Bader, D., Flanner, M., Foucar, J. G., Jacob, R., Keen,  
910 N., Klein, S. A., Liu, X., Salinger, A. G., Shrivastava, M., and Yang, Y.: An Overview of the  
911 Atmospheric Component of the Energy Exascale Earth System Model, *J. Adv. Model. Earth*  
912 *Syst.*, 11, 2377–2411, <https://doi.org/10.1029/2019MS001629>, 2019.  
913  
914 Rickly, P. S., Xu, L., Crouse, J. D., Wennberg, P. O., and Rollins, A. W.: Improvements to a  
915 laser-induced fluorescence instrument for measuring SO<sub>2</sub> – impact on accuracy and precision,  
916 *Atmos. Meas. Tech.*, 14, 2429–2439, <https://doi.org/10.5194/amt-14-2429-2021>, 2021.  
917  
918 Rienecker, M., Suarez, M., Todling, R., Bacmeister, J., Takacs, L., Liu, H.-C., Gu, W.,  
919 Sienkiewicz, M., Koster, R., Gelaro, R., Stajner, I., and Nielsen, J.: The GEOS-5 Data  
920 Assimilation System – Documentation of Versions 5.0.1, 5.1.0, and 5.2.0., Vol. 27 of Technical  
921 Report Series on Global Modeling and Data Assimilation, NASA Goddard Space Flight Center,  
922 Greenbelt, MD, USA, 2008.  
923  
924 Rissman, T. A., Nenes, A., and Seinfeld, J. H.: Chemical amplification (or dampening) of the  
925 Twomey effect: Conditions derived from droplet activation theory, *J. Atmos. Sci.*, 61(8), 919–  
926 930, [https://doi.org/10.1175/1520-0469\(2004\)061<0919:CAODOT>2.0.CO;2](https://doi.org/10.1175/1520-0469(2004)061<0919:CAODOT>2.0.CO;2), 2004.  
927



- 928 Rollins, A. W., Thornberry, T. D., Ciciora, S. J., McLaughlin, R. J., Watts, L. A., Hanisco, T. F.,  
929 Baumann, E., Giorgetta, F. R., Bui, T. V., Fahey, D. W., and Gao, R.-S.: A laser-induced  
930 fluorescence instrument for aircraft measurements of sulfur dioxide in the upper troposphere and  
931 lower stratosphere, *Atmos. Meas. Tech.*, 9, 4601–4613, [https://doi.org/10.5194/amt-9-4601-](https://doi.org/10.5194/amt-9-4601-2016)  
932 2016, 2016.  
933
- 934 Schueneman, M. K., Nault, B. A., Campuzano-Jost, P., Jo, D. S., Day, D. A., Schroder, J. C.,  
935 Palm, B. B., Hodzic, A., Dibb, J. E., and Jimenez, J. L.: Aerosol pH indicator and organosulfate  
936 detectability from aerosol mass spectrometry measurements, *Atmos. Meas. Tech.*, 14, 2237–  
937 2260, 2021.  
938
- 939 Seinfeld, J. H., Bretherton, C., Carslaw, K. S., Coe, H., DeMott, P. J., Dunlea, E. J., Feingold, G.,  
940 Ghan, S., Guenther, A. B., Kahn, R., Kraucunas, I., Kreidenweis, S. M., Molina, M. J., Nenes,  
941 A., Penner, J. E., Prather, K. A., Ramanathan, V., Ramaswamy, V., Rasch, P. J., Ravishankara,  
942 A. R., Rosenfeld, D., Stephens, G., and Wood, R.: Improving our fundamental understanding of  
943 the role of aerosol–cloud interactions in the climate system, *P. Natl. Acad. Sci. USA*, 113, 5781–  
944 5790, <https://doi.org/10.1073/pnas.151404311>, 2016.  
945
- 946 Schulz, M., Textor, C., Kinne, S., Balkanski, Y., Bauer, S., Berntsen, T., Berglen, T., Boucher,  
947 O., Dentener, F., Guibert, S., Isaksen, I. S. A., Iversen, T., Koch, D., Kirkevåg, A., Liu, X.,  
948 Montanaro, V., Myhre, G., Penner, J. E., Pitari, G., Reddy, S., Seland, Ø., Stier, P., and  
949 Takemura, T.: Radiative forcing by aerosols as derived from the AeroCom present-day and pre-  
950 industrial simulations, *Atmos. Chem. Phys.*, 6, 5225–5246, [https://doi.org/10.5194/acp-6-5225-](https://doi.org/10.5194/acp-6-5225-2006)  
951 2006, 2006  
952
- 953 Simpson, I. J., Colman, J. J., Swanson, A. L., Bandy, A. R., Thornton, D. C., Blake, D. R., and F.  
954 S. Rowland, F. S.: Aircraft Measurements of Dimethyl Sulfide (DMS) Using a Whole Air  
955 Sampling Technique, *J. Atmos. Chem.*, 39, 191–213, <https://doi.org/10.1023/A:1010608529779>,  
956 2001.  
957
- 958 Slingo, J.: The development and verification of a cloud prediction scheme for the ECMWF  
959 model, *Q. J. Roy. Meteor. Soc.*, 113, 899–927, <https://doi.org/10.1002/qj.49711347710>, 1987.  
960
- 961 Smith, R. N. B.: A scheme for predicting layer clouds and their water content in a general  
962 circulation model, *Q. J. Roy. Meteor. Soc.*, 116, 435–460,  
963 <https://doi.org/10.1002/qj.49711649210>, 1990.  
964
- 965 Søvde, O. A., Prather, M. J., Isaksen, I. S. A., Berntsen, T. K., Stordal, F., Zhu, X., Holmes, C.  
966 D., and Hsu, J.: The chemical transport model Oslo CTM3, *Geosci. Model Dev.*, 5, 1441–1469,  
967 <https://doi.org/10.5194/gmd-5-1441-2012>, 2012.  
968
- 969 Tan, J., Fu, J. S., Dentener, F., Sun, J., Emmons, L., Tilmes, S., Flemming, J., Takemura, T.,  
970 Bian, H., Zhu, Q., Yang, C.-E., and Keating, T.: Source contributions to sulfur and nitrogen  
971 deposition – an HTAP II multi-model study on hemispheric transport, *Atmos. Chem. Phys.*, 18,  
972 12223–12240, <https://doi.org/10.5194/acp-18-12223-2018>, 2018.  
973



- 974 Tiedtke, M.: Representation of clouds in large-scale models, *Mon. Weather Rev.*, 121, 3040–  
975 3061, [https://doi.org/10.1175/1520-0493\(1993\)121<3040:ROCILS>2.0.CO;2](https://doi.org/10.1175/1520-0493(1993)121<3040:ROCILS>2.0.CO;2), 1993.  
976
- 977 Wang, H., Easter, R. C., Zhang, R., Ma, P., Singh, B., Zhang, K., Ganguly, D., Rasch, P. J.,  
978 Burrows, S. M., Ghan, S. J., Lou, S., Qian, Y., Yang, Y., Feng, Y., Flanner, M., Leung, L. R.,  
979 Liu, X., Shrivastava, M., Sun, J., Tang, Q., Xie, S., and Yoon, J.: Aerosols in the E3SM Version  
980 1: New Developments and Their Impacts on Radiative Forcing, *J. Adv. Model. Earth Syst.*, 12,  
981 e2019MS001851, <https://doi.org/10.1029/2019MS001851>, 2020.  
982
- 983 Wang, D., Zhu, B., Wang, H., and Sun, L., Simulation study on the indirect effect of sulfate on  
984 the summer climate over the eastern China monsoon region, *Sci. Rep.*, 11, 8295,  
985 <https://doi.org/10.1038/s41598-021-87832-5>, 2021.  
986
- 987 Williamson, C. J., Kupc, A., Axisa, D., Bilsback, K. R. Bui, T. P., Campuzano-Jost, P., Dollner,  
988 M., Froyd, K. D., Hodshire, A. L., Jimenez, J. L., Kodros, J. K., Luo, G., Murphy, D. M., Nault,  
989 B. A., Ray, E. A., Weinzierl, B., Wilson, J. C., Yu, F., Yu, P., Pierce, J. R., and Brock, C. A.: A  
990 large source of cloud condensation nuclei from new particle formation in the tropics, *Nature*,  
991 574, 399–403, <https://doi.org/10.1038/s41586-019-1638-9>, 2019.  
992
- 993 Thompson, C. R., Wofsy, S. C., Prather, M. J., Newman, P. A., Hanisco, T. F., Ryerson, T. B.,  
994 Fahey, D. W., Apel, E. C., Brock, C. A., Brune, W. H., Froyd, K., Katich, J. M., Nicely, J. M.,  
995 Peischl, J., Ray, E., Veres, P. R., Wang, S., Allen, H. M., Asher, E., Bian, H., Blake, D.,  
996 Bourgeois, I., Budney, J., Paul Bui, T., Butler, A., Campuzano-Jost, P., Chang, C., Chin, M.,  
997 Commane, R., Correa, G., Crounse, J. D., Daube, B., Dibb, J. E., Digangi, J. P., Diskin, G. S.,  
998 Dollner, M., Elkins, J. W., Fiore, A. M., Flynn, C. M., Guo, H., Hall, S. R., Hannun, R. A., Hills,  
999 A., Hints, E. J., Hodzic, A., Hornbrook, R. S., Greg Huey, L., Jimenez, J. L., Keeling, R. F.,  
1000 Kim, M. J., Kupc, A., Lacey, F., Lait, L. R., Lamarque, J.-F., Liu, J., Mckain, K., Meinardi, S.,  
1001 Miller, D. O., Montzka, S. A., Moore, F. L., Morgan, E. J., Murphy, D. M., Murray, L. T., Nault,  
1002 B. A., Andrew Neuman, J., Nguyen, L., Gonzalez, Y., Rollins, A., Rosenlof, K., Sargent, M.,  
1003 Schill, G., Schwarz, J. P., St. Clair, J. M., Steenrod, S. D., Stephens, B. B., Strahan, S. E., Strode,  
1004 S. A., Sweeney, C., Thames, A. B., Ullmann, K., Wagner, N., Weber, R., Weinzierl, B.,  
1005 Wennberg, P. O., Williamson, C. J., Wolfe, G. M., and Zeng, L.: THE NASA ATMOSPHERIC  
1006 TOMOGRAPHY (ATom) MISSION: Imaging the Chemistry of the Global Atmosphere, *Bull.*  
1007 *Am. Meteorol. Soc.*, 103, E761-E790, <https://doi.org/10.1175/BAMS-D-20-0315.1>, 2022.  
1008
- 1009 Zhang, K., Zhang, W., Wan, H., Rasch, P. J., Ghan, S. J., Easter, R. C., Shi, X., Wang, Y.,  
1010 Wang, H., Ma, P.-L., Zhang, S., Sun, J., Burrows, S. M., Shrivastava, M., Singh, B., Qian, Y.,  
1011 Liu, X., Golaz, J.-C., Tang, Q., Zheng, X., Xie, S., Lin, W., Feng, Y., Wang, M., Yoon, J.-H.,  
1012 and Leung, L. R.: Effective radiative forcing of anthropogenic aerosols in E3SM version 1:  
1013 historical changes, causality, decomposition, and parameterization sensitivities, *Atmos. Chem.*  
1014 *Phys.*, 22, 9129–9160, <https://doi.org/10.5194/acp-22-9129-2022>, 2022.  
1015
- 1016 Zhu, J., Penner, J. E., Lin, G., Zhou, C., Xu, L., and Zhuang, B.: Mechanism of SOA formation  
1017 determines magnitude of radiative effects. *Proceedings of the National Academy of Sciences of*  
1018 *the United States of America*, 114, 12685–12690, [https://doi.org/10.1073/](https://doi.org/10.1073/pnas.1712273114)  
1019 [pnas.1712273114](https://doi.org/10.1073/pnas.1712273114), 2017.  
1020



1021 Zhu, J., Penner, J. E., Yu, F., Sillman, S., Andreae, M. O., and Coe, H.: Decrease in radiative  
1022 forcing by organic aerosol nucleation, climate, and land use change. *Nature Commun.*, 10, 423,  
1023 <https://doi.org/10.1038/s41467-019-08407-7>, 2019.  
1024  
1025  
1026  
1027  
1028  
1029  
1030  
1031  
1032  
1033  
1034  
1035  
1036  
1037  
1038  
1039  
1040  
1041  
1042  
1043  
1044  
1045  
1046  
1047  
1048  
1049  
1050  
1051  
1052  
1053  
1054  
1055  
1056  
1057  
1058  
1059  
1060  
1061  
1062  
1063  
1064  
1065  
1066



1067 Table 1. ATom sulfur measurements used in the study

Instrument	SO <sub>4</sub>		SO <sub>2</sub>		MSA		DMS	
	AMS <sup>a</sup>	PALMS <sup>b</sup>	CIMS <sup>c</sup>	LIF <sup>d</sup>	AMS	PALMS	TOGA <sup>e</sup>	WAS <sup>f</sup>
ATom deployment(s)	1 to 4	1 to 4	1 to 4	4	1 to 4	1 to 4	2 to 4	1 to 4
Frequency	60 s	180 s	1 s	1 s	1 s	180 s	120 s	Variable but ~180 s
Accuracy	±35% (2s)	±60% at 10 ng m <sup>-3</sup> ±20% at 1 µg m <sup>-3</sup>	±25%	± 9% (1s)	±35% (2s)	±70%	15% or better	15%
precision			130pptv					10%
Detection limit	5-15 ng sm <sup>-3</sup>	~10 ng sm <sup>-3</sup>		2 pptv	2.5 ng sm <sup>-3</sup> (60 s)	~15 ng sm <sup>-3</sup>	1 ppt	1 ppt
Cut-off size (dry diameter)	~0.75 µm	0.1-3 µm			~0.75 µm	0.1-3 µm		
Primary Investigator(s)	Jose Jimenez and Pedro Campuzano Jost	Karl Froyd and Gregory Schill	Paul Wennberg	Andrew Rollins	Jose Jimenez and Pedro Campuzano Jost	Karl Froyd and Gregory Schill	Eric Apel	Donald Blake
References	Guo et al., 2021; Schueneman et al., 2021	Froyd et al., 2019	Allen et al., 2022; Crouse et al., 2006	Rollins et al., 2016	Hodshire et al., 2019	Froyd et al., 2019	Apel et al., 2015	Simpson et al., 2001

1068 <sup>a</sup>AMS: Aerosol Mass Spectrometer  
 1069 <sup>b</sup>PALMS: Particle Analysis by Laser Mass Spectrometry  
 1070 <sup>c</sup>CIMS: Chemical Ionization Mass Spectrometer  
 1071 <sup>d</sup>LIF: Laser Induced Fluorescence  
 1072 <sup>e</sup>TOGA: NCAR Trace Organic Gas Analyzer  
 1073 <sup>f</sup>WAS: Whole Air Sampler

1074  
1075  
1076 Table 2. AeroCom Models used in this study

Model Abbreviation	Model Version	Nominal Resolution	Vertical Levels	Meteorological Fields	Ocean Surface Temperature Data	Interactive Aerosol-Meteorology	Endogenous Oxidants	Endogenous DMS Emission	Aerosol Module	Anthropogenic Emission	Volcano Emission	Key References
CAM-ATRAS	CAM5-ATRAS2	1.9° × 2.5°	30	MERRA-2	HadSST	Yes	Yes	No	Microphysics, 12 sectional size bins, and internal mixing of aerosol constituents in each bin.	CEDS (Hoesly et al., 2018),	Degassing (Andres and Kasgnoc, 1998), Eruption (Neely and Schmidt, 2016)	Liu and Matsui 2021; Matsui 2017; Matsui and Mahowald, 2017
E3SM	v1.0	1° × 1°	72	ERA-Interim	HadSST	Yes	No	No	Microphysics, MAM4, internal mixing within a mode, external mixing between modes	CEDS (Hoesly et al., 2018)	Continuous emission (Denener et al., 2006), No eruptive emissions.	Rasch et al., 2019; Wang et al., 2020; Zhang et al. 2022
GEOS	Icarus-3 3 p2	1° × 1°	72	MERRA-2	MERRA sst	Yes	No	Yes	GOCART, Bulk, external mixing	CEDS (Hoesly et al., 2018)	Carns et al., 2016, 2017	Bian 2017; Colarco et al., 2010; Chin et al., 2000
IMPACT		1.9° × 2.5°	30	Open IFS ECMWF	HadSST	No	Yes	no	Microphysics, internal mixing within a mode, external mixing between modes	CEDS (Hoesly et al., 2018)	AeroCom volcanic emissions	Zhu et al., 2017; Zhu et al., 2019
OsloCTM3	OsloCTM3v1.02	2.25° × 2.25°	60	Open IFS ECMWF	Open IFS ECMWF	No	Yes	Yes	Bulk, external mixing	SSP245 with linear interpolation for 2017	AeroCom volcanic emissions (busing TOMS- and OMI-based estimates), continuous from Dentener (2006)	Lund et al., 2018; Sovde et al., 2012

1077  
1078  
1079  
1080  
1081  
1082  
1083  
1084



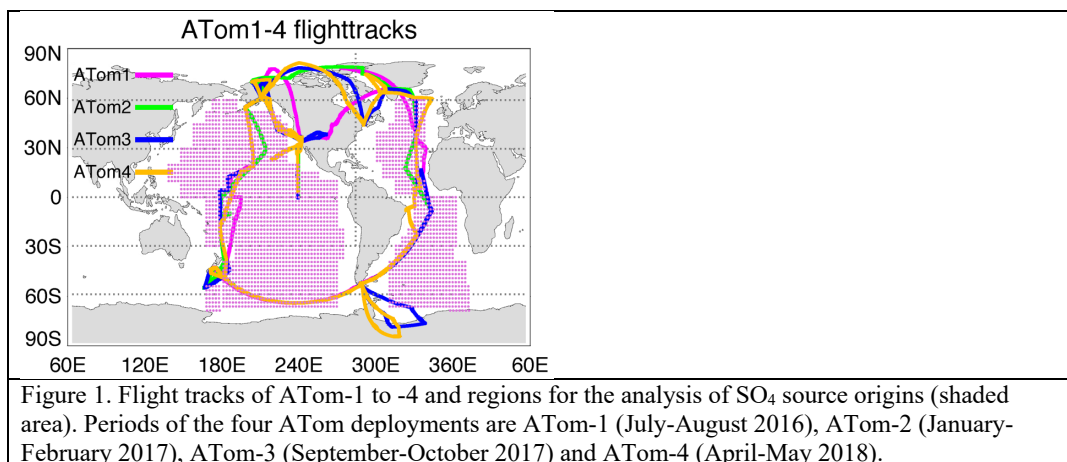


1085 Table 3. Global sulfur budget in 2017

		Emission	SUPSO <sub>2</sub> <sup>1</sup>	SUPMSA	SUPSO <sub>4</sub>	Dry	Wet	TotalSource	Burden	Lifetime
		TgS/yr	TgS/yr	TgS/yr	TgS/yr	TgS/yr	TgS/yr	TgS/yr	TgS	days
CAM-ATRAS	DMS	26.05	-26.05	--	--	--	--	26.05	0.13	1.8
	SO <sub>2</sub>	68.67	26.05	--	-55.67	-39.05	--	94.72	0.445	1.7
	SO <sub>4</sub>	1.76	--	--	55.67	-4.72	-53.23	58.09	0.67	4.2
E3SM	DMS	19.43	-19.40	--	--	--	--	19.43	0.0658	1.24
	SO <sub>2</sub>	67.92	19.40	--	-38.56	-48.76	--	87.32	0.3825	1.60
	SO <sub>4</sub>	1.74	--	--	38.56	-6.95	-33.31	40.31	0.6183	5.60
GEOS	DMS	15.57	-14.84	-0.74	--	--	--	15.57	0.0252	0.59
	SO <sub>2</sub>	67.06	14.84	--	-37.49	-32.93	-11.39	81.90	0.3488	1.55
	SO <sub>4</sub>	1.68	--	--	37.49	-5.27	-33.90	39.17	0.3269	3.05
	MSA	--	--	0.74	--	-0.10	-0.64	-0.74	0.0063	3.11
IMPACT	DMS	18.22	-18.22	--	--	--	--	18.05	0.0369	0.75
	SO <sub>2</sub>	64.76	18.22	--	-51.44	-31.29	--	82.98	0.4134	1.82
	SO <sub>4</sub>	1.36	--	--	51.44	-3.48	-49.32	52.80	0.7502	5.19
OsloCTM3	DMS	26.93	-26.93	--	--	--	--	26.93	0.1496	2.03
	SO <sub>2</sub>	52.80	26.93	--	-49.23	-29.01	-1.49	79.73	0.2346	1.08
	SO <sub>4</sub>	1.053	--	--	55.49	-6.35	-50.29	56.54	0.8681	5.60

<sup>1</sup>SUPSO<sub>2</sub>: chemical production for SO<sub>2</sub>

1086  
 1087  
 1088  
 1089  
 1090  
 1091  
 1092  
 1093  
 1094  
 1095  
 1096  
 1097  
 1098  
 1099  
 1100  
 1101  
 1102  
 1103  
 1104  
 1105  
 1106  
 1107  
 1108  
 1109  
 1110  
 1111  
 1112  
 1113  
 1114  
 1115  
 1116  
 1117  
 1118



1119  
1120  
1121  
1122  
1123  
1124  
1125  
1126  
1127  
1128  
1129  
1130  
1131  
1132  
1133  
1134  
1135  
1136  
1137  
1138  
1139  
1140  
1141  
1142  
1143  
1144  
1145  
1146  
1147  
1148  
1149  
1150

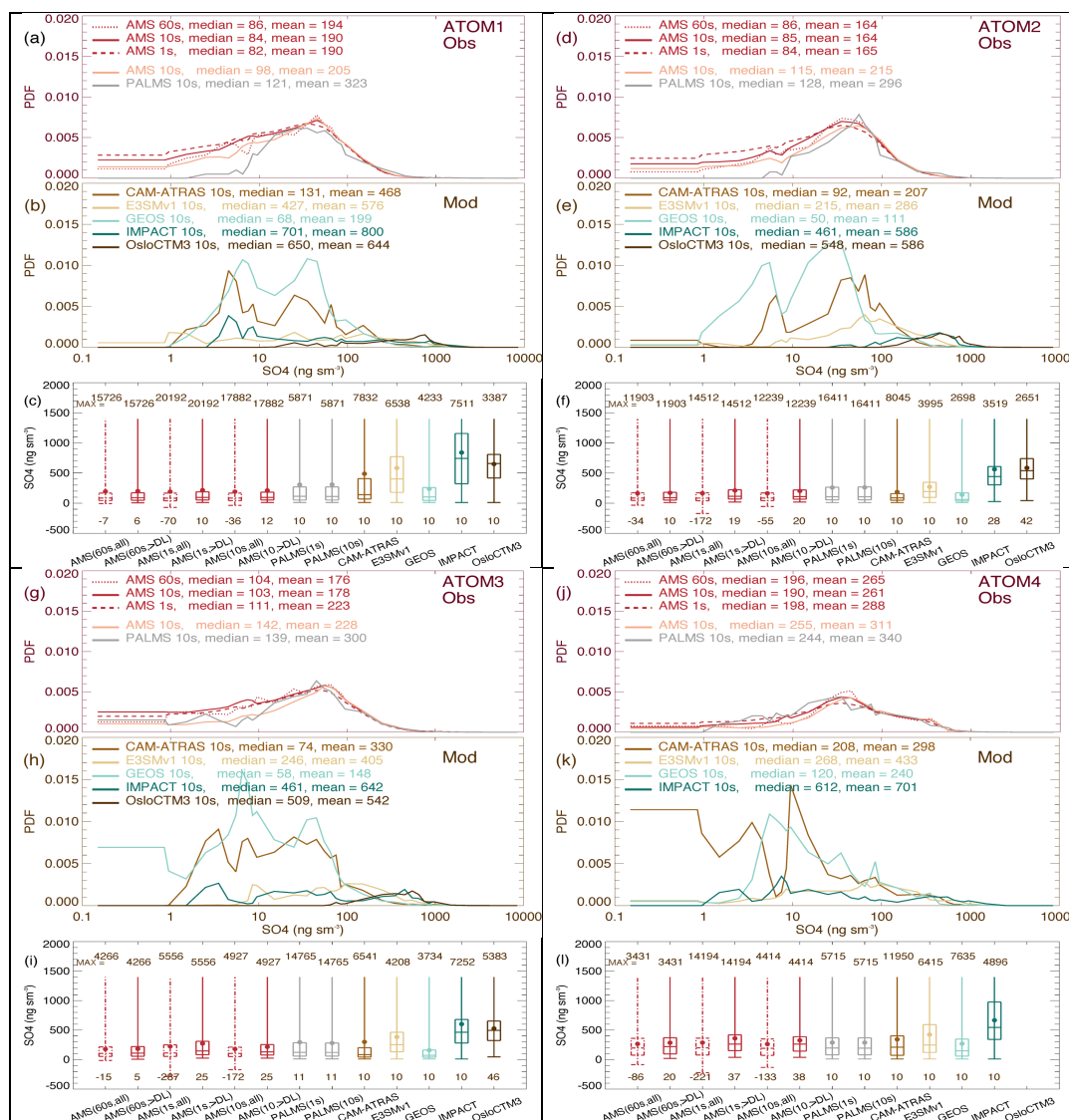


Figure 2. Probability density function (PDF) of  $\text{SO}_4$  from AMS and PALMS observations (a, d, g, j) and five model simulations (b, e, h, k), as well as their statistical values shown in box-and-whisker plot (c, f, i, l) for four ATom deployments. PDF analyses include AMS  $\text{SO}_4$  reported in three-time frequencies (1-s, 10-s, and 60-s) in red. Data for all other colors are sampled at 10-s points where all instrument measurements are available. The median/mean values listed are calculated when the measured values are above the detection limit. Statistical values include the range of data from the minimum to the maximum values, the three levels in boxes for 25th, 50th (aka median value), and 75th percentiles, and the filled circles for mean values. Box-and-whisker in red dot-dash is for all AMS sampling points including negative values, and in red solid is for sampling points when AMS values exceeded detection limit (DL).

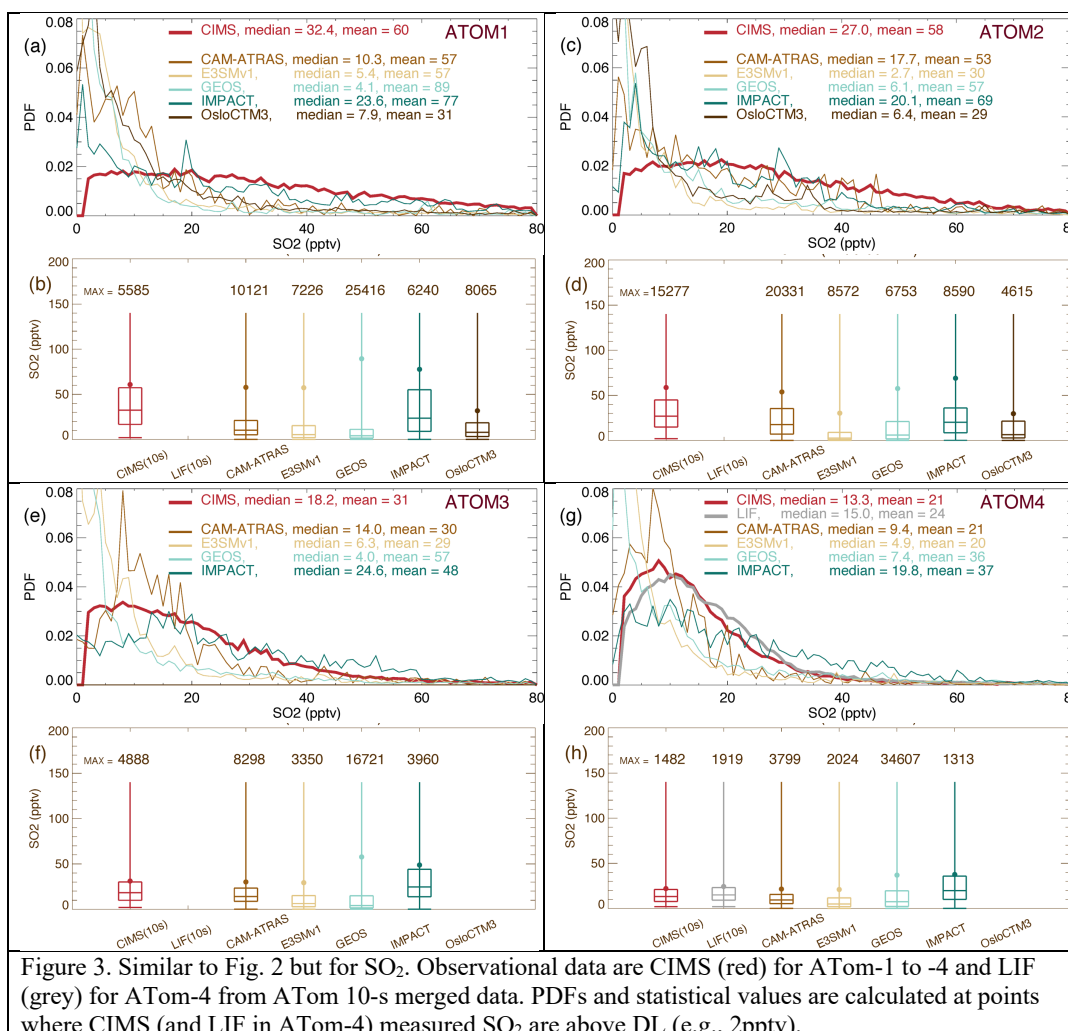


Figure 3. Similar to Fig. 2 but for SO<sub>2</sub>. Observational data are CIMS (red) for ATom-1 to -4 and LIF (grey) for ATom-4 from ATom 10-s merged data. PDFs and statistical values are calculated at points where CIMS (and LIF in ATom-4) measured SO<sub>2</sub> are above DL (e.g., 2pptv).

1152  
 1153  
 1154  
 1155  
 1156  
 1157  
 1158  
 1159  
 1160  
 1161  
 1162  
 1163

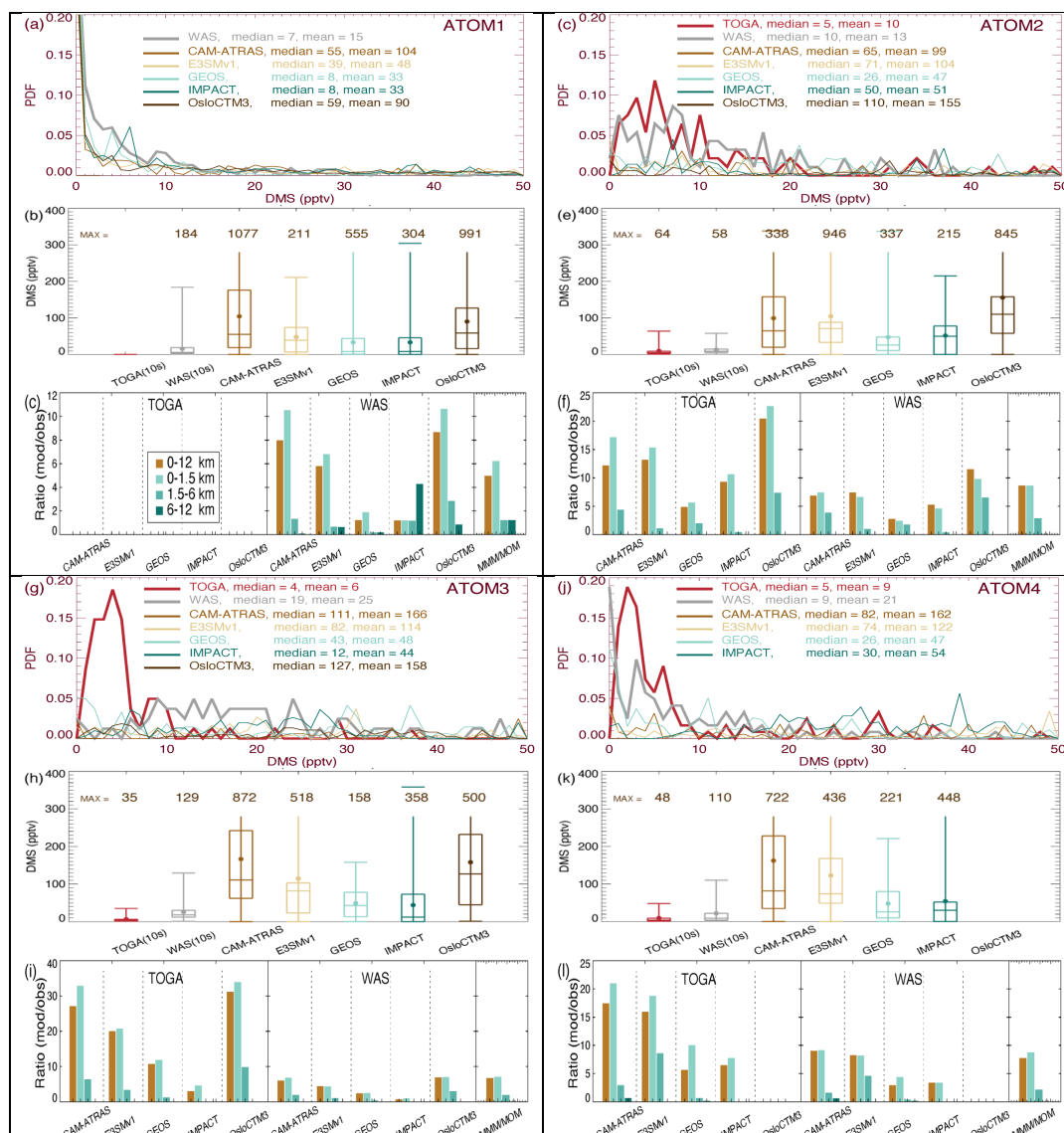
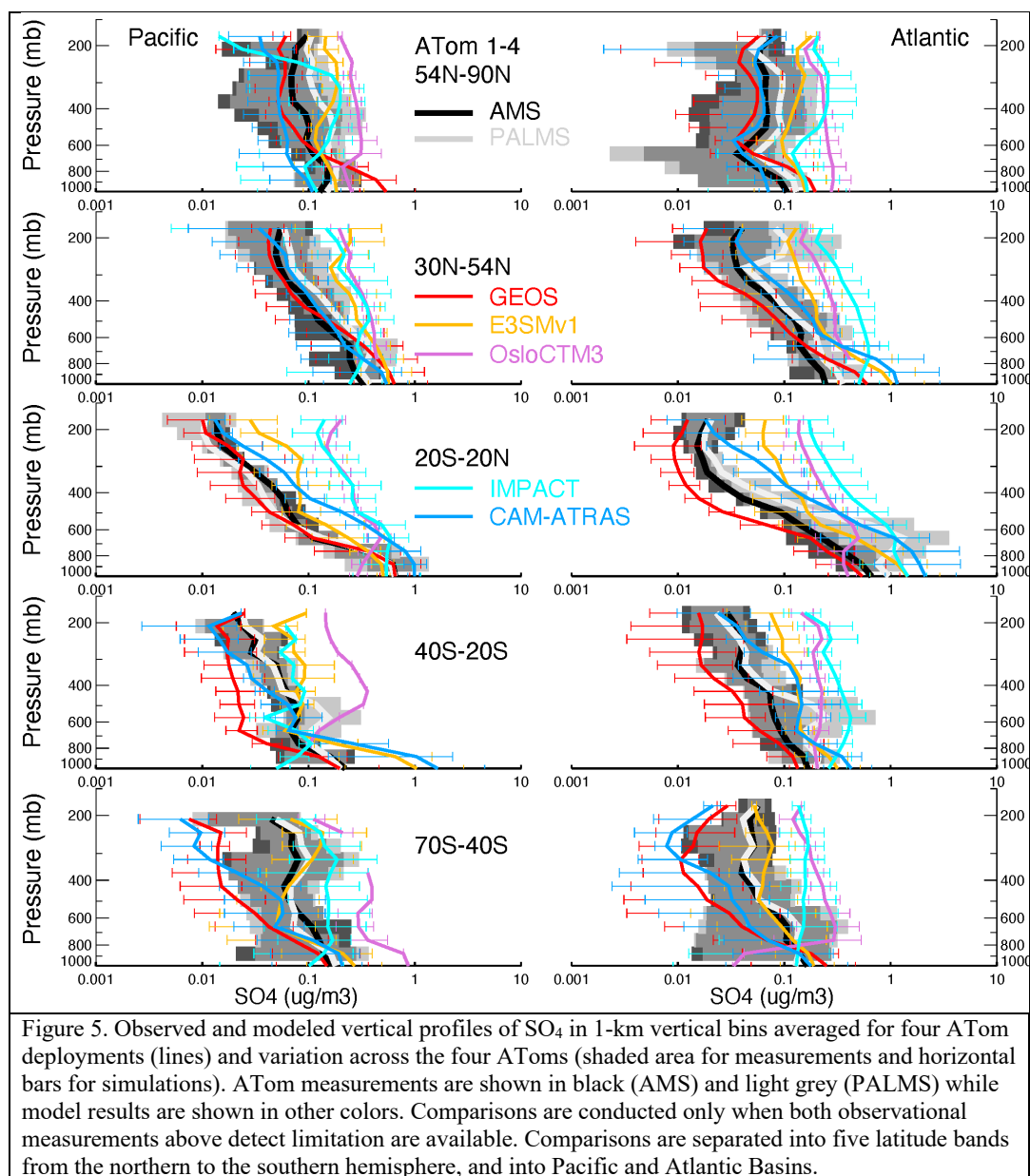


Figure 4. Similar to Fig. 2 but for DMS for ATom-1 (a,b), ATom-2 (d,e), ATom-3 (g,h), and ATom-4 (j,k). (c, f, i, and l) Ratio of DMS median values between model simulation and observation for four ATom deployments. Ratio analyses are performed on four vertical ranges as shown in four colors (see legend in (c)). The last column “MMM/MOM” refers to multi-model median to multi-observation median. The original data reported by TOGA and by WAS have also been converted to 10-s frequency. Data included in PDF and statistical analysis are on 10-s points where DMS measured by both TAGO and WAS are above DL (i.e., 1 pptv).

1164  
 1165



1166  
1167  
1168  
1169  
1170  
1171

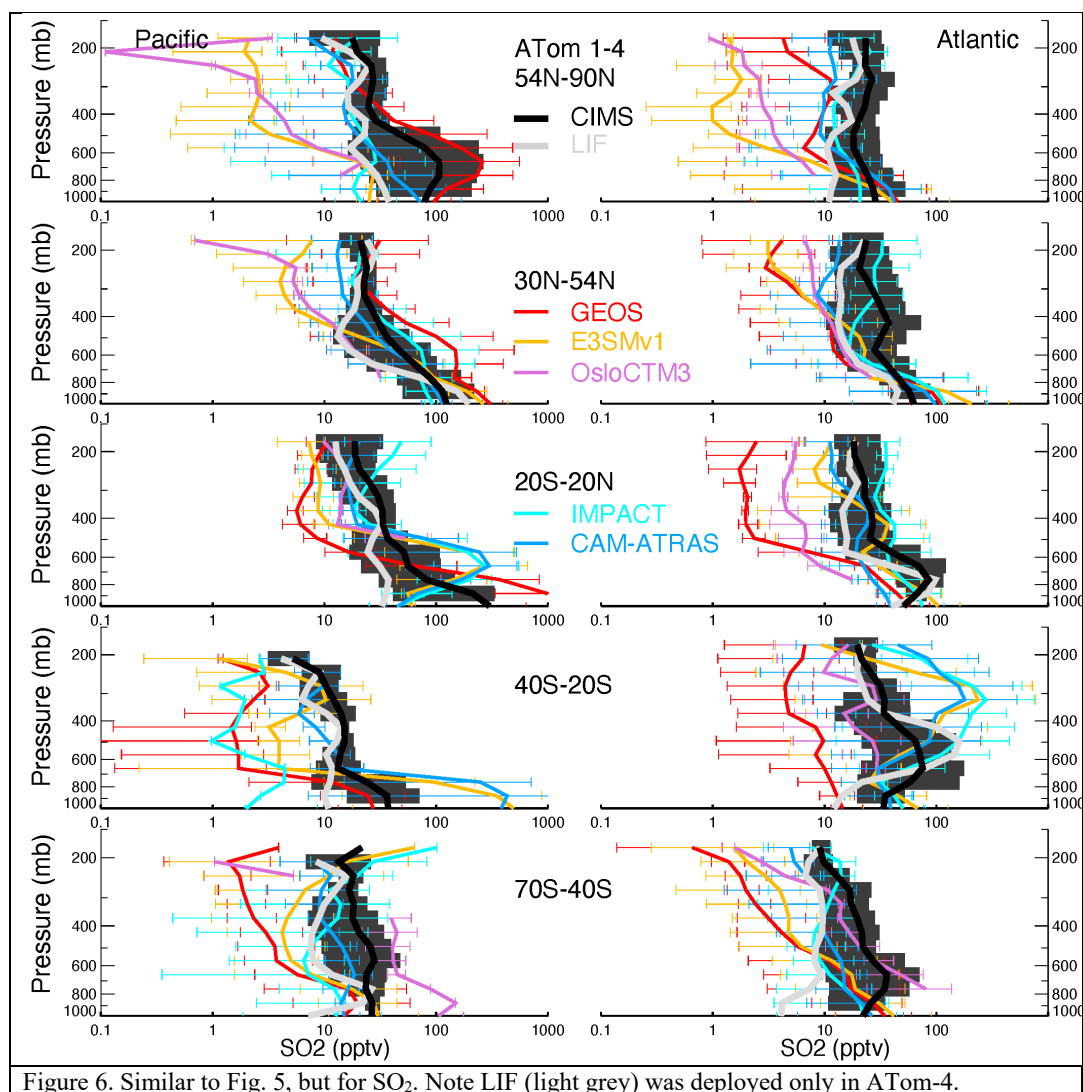
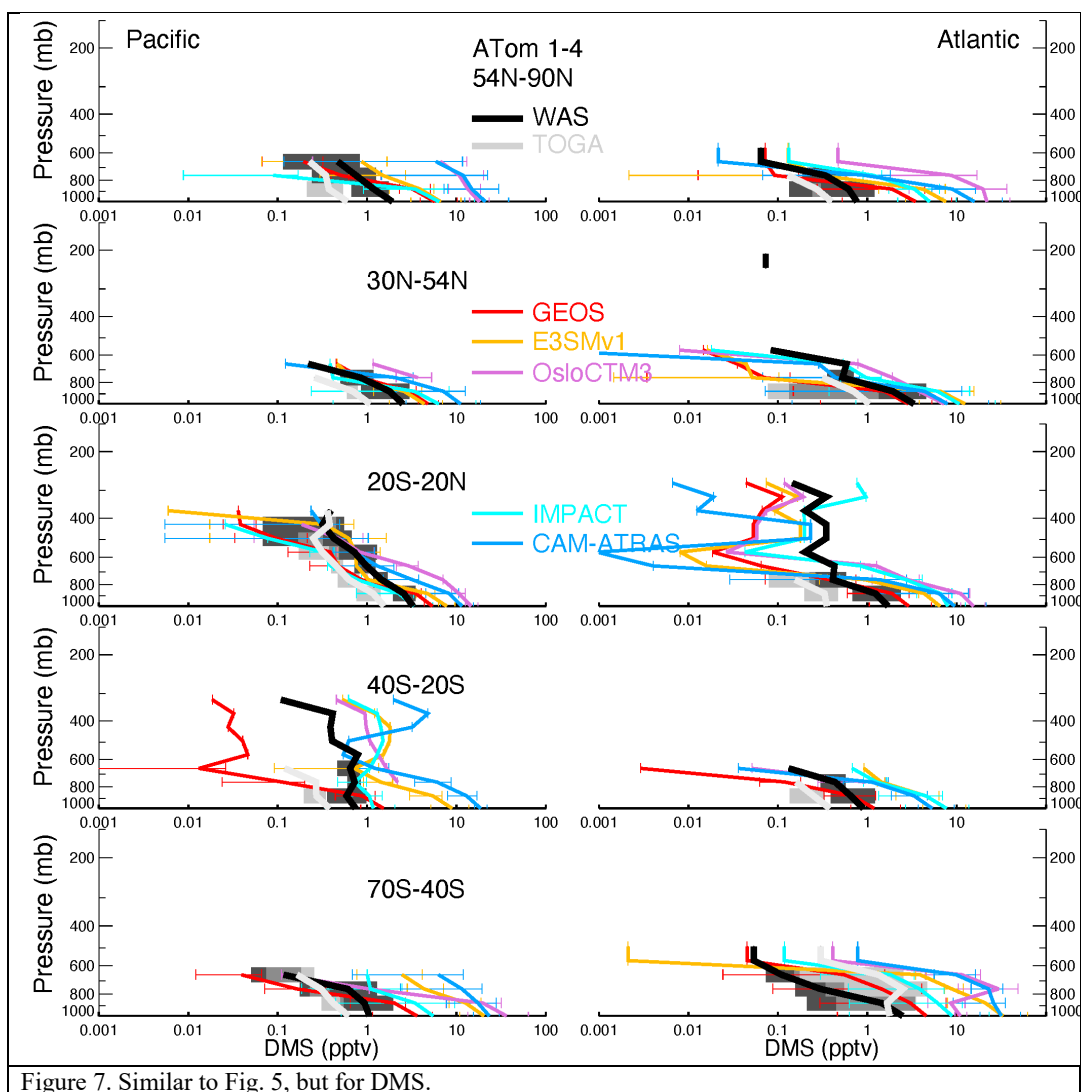


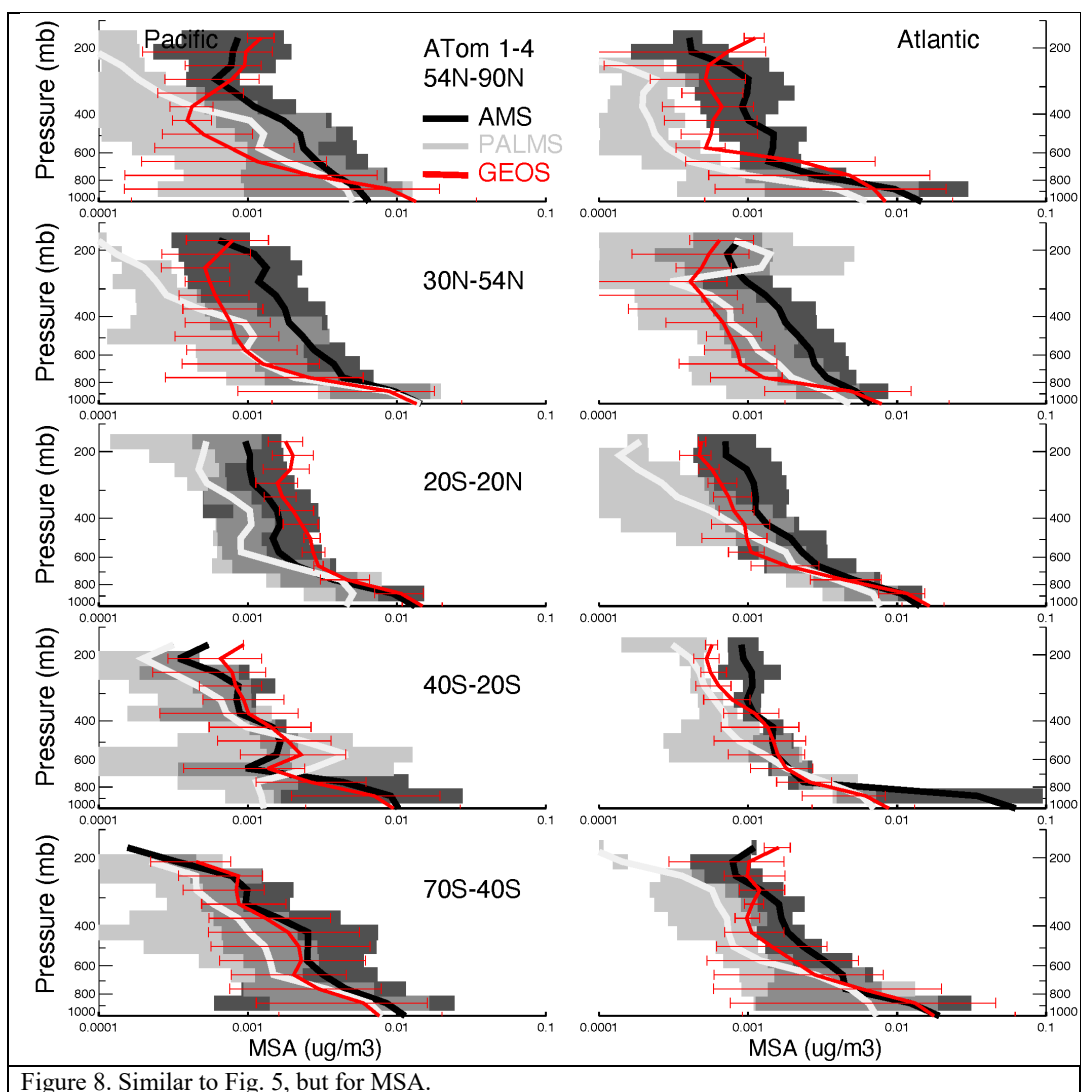
Figure 6. Similar to Fig. 5, but for SO<sub>2</sub>. Note LIF (light grey) was deployed only in ATom-4.

1172  
1173  
1174  
1175  
1176  
1177  
1178  
1179  
1180  
1181  
1182

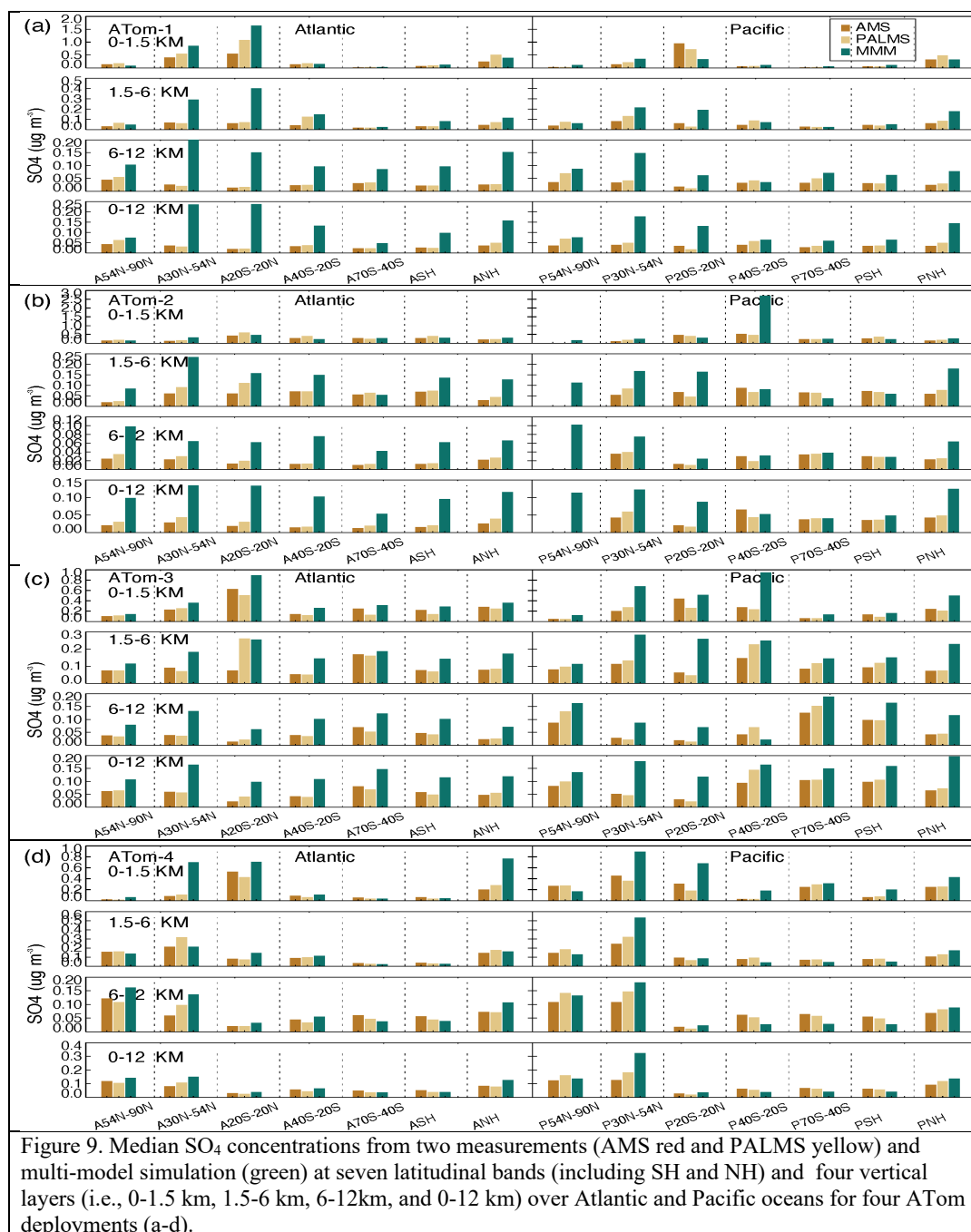


1183  
1184  
1185  
1186





1187  
1188  
1189  
1190  
1191  
1192  
1193



1194  
 1195  
 1196

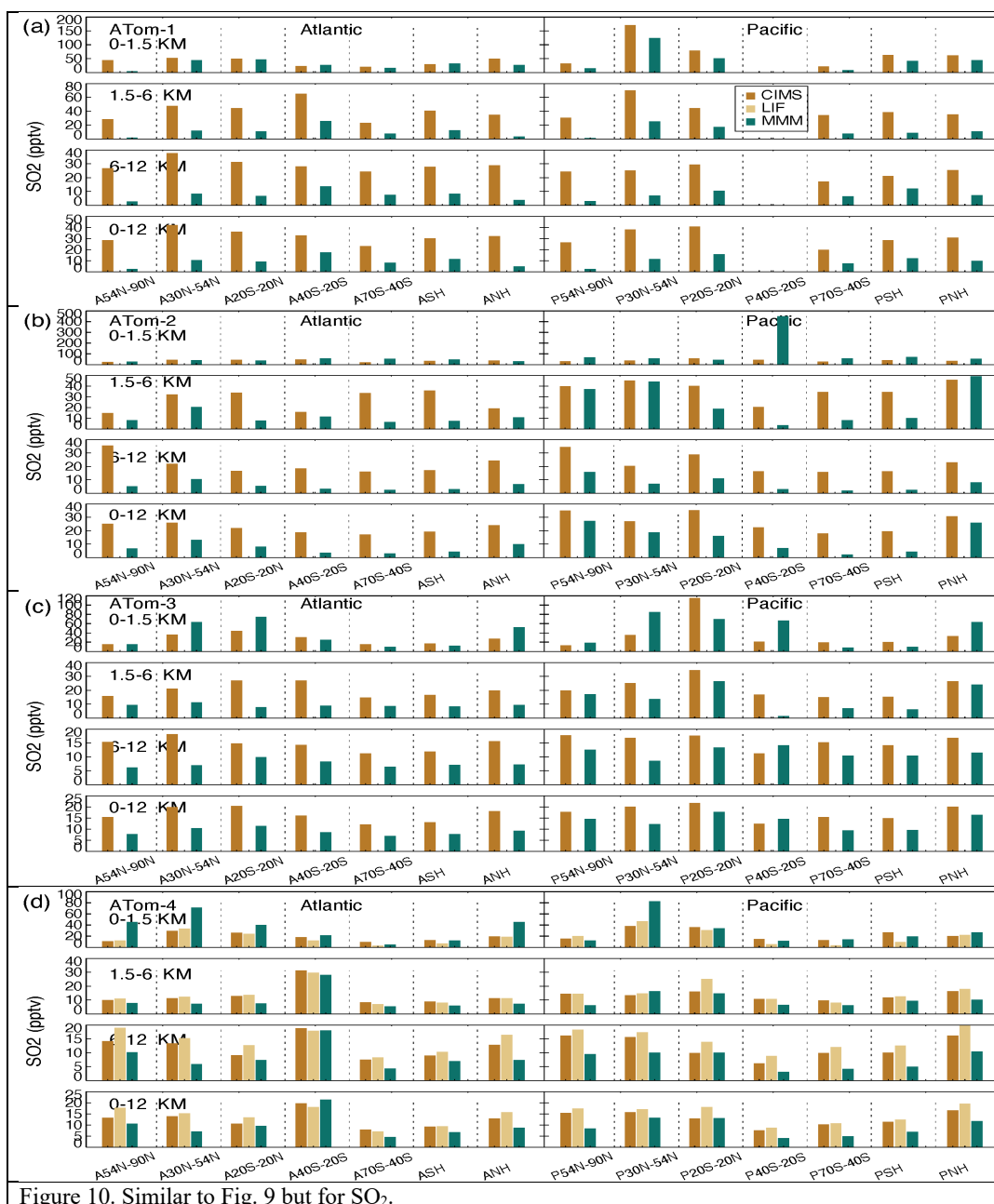


Figure 10. Similar to Fig. 9 but for SO<sub>2</sub>.

1197  
 1198  
 1199  
 1200  
 1201

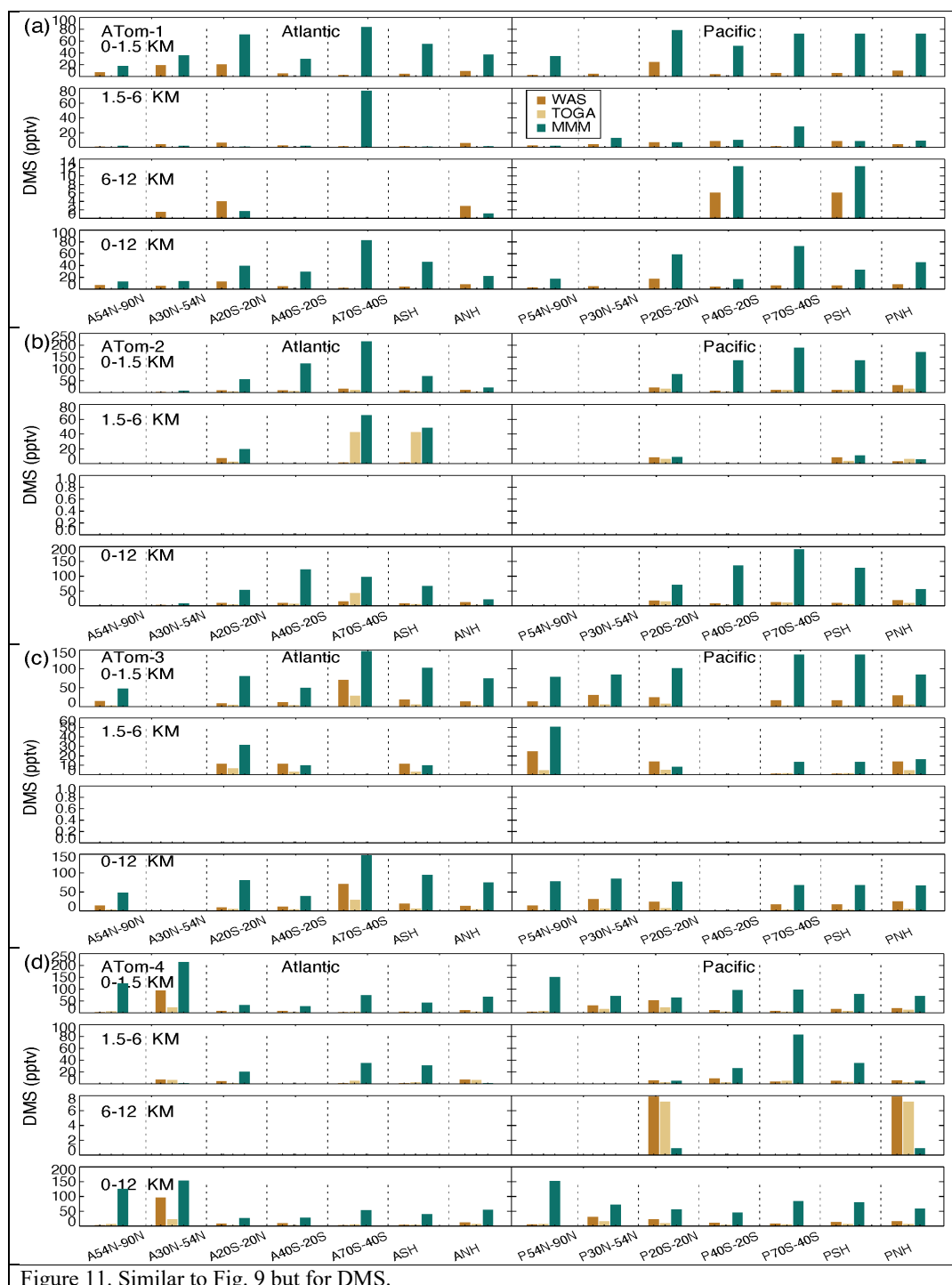
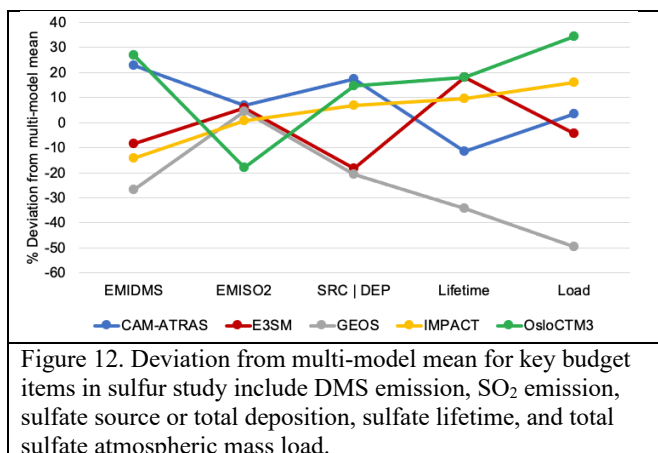


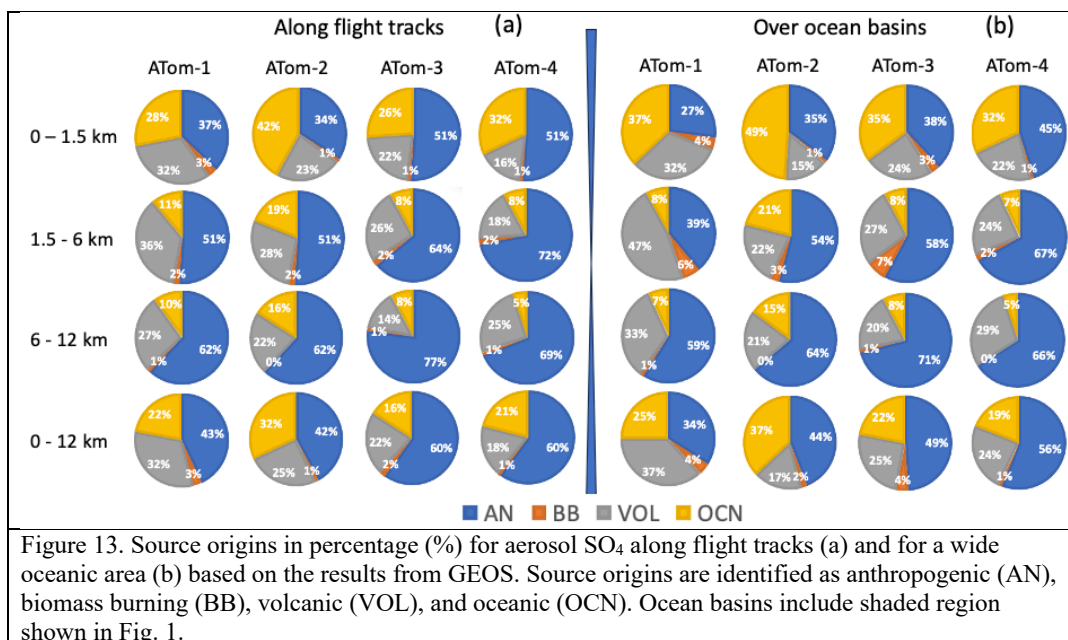
Figure 11. Similar to Fig. 9 but for DMS.



1203



1204  
1205



1206